European Cells and Materials Vol.58 2026 (pages 158–180) DOI: 10.22203/eCM.v058a12 ISSN 1473-2262

Original Article

Photocrosslinked PEG-PVP-Pullulan Composites Reinforced With Brushite: A Preliminary Bone-Facing Material for Osteochondral Tissue Engineering

Karina Niziołek[1,2,*], Dagmara Słota[2], Katarzyna Haraźna[2] and Agnieszka Sobczak-Kupiec[2]

[1]Cracow University of Technology, CUT Doctoral School, Faculty of Materials Engineering and Physics, Department of Materials Science, 37 Jana Pawła II Av., 31-864 Krakow, Poland

[2]Cracow University of Technology, Faculty of Materials Engineering and Physics, Department of Materials Science, 37 Jana Pawła II Av., 31-864 Krakow, Poland

Abstract

Objectives: The development of biomaterials for bone tissue engineering requires a combination of suitable mechanical properties, bioactivity, and cytocompatibility. In this study, photocrosslinked polymer-ceramic composites based on poly(vinylpyrrolidone) (PVP), poly(ethylene glycol) (PEG), and pullulan were developed and reinforced with dicalcium phosphate dihydrate (DCPD, brushite) to obtain bioactive materials with enhanced biological performance. **Methods:** DCPD was synthesized via a wet precipitation method and incorporated into polymer matrices through UV-induced photopolymerization. The resulting composites were characterized in terms of swelling behavior, hardness, degradation in physiological conditions, surface morphology, and biological response. Cytocompatibility was assessed using direct and indirect cytotoxicity assays, proliferation studies, and scanning electron microscopy (SEM) evaluation of MC3T3-E1 preosteoblast adhesion and morphology. **Results:** The composition of the polymer matrix significantly affected the physicochemical properties of the materials. Increased PVP content resulted in higher hardness and more developed surface morphology, whereas DCPD incorporation reduced swelling and increased surface roughness. All materials exhibited satisfactory cytocompatibility, with cell viability remaining above the threshold specified by ISO 10993-5. Proliferation studies demonstrated progressive cell growth over time, particularly on DCPD-containing composites. SEM observations confirmed successful cell attachment and favorable cell-material interactions, with the most pronounced response observed for balanced PVP/PEG formulations reinforced with DCPD. **Conclusions:** The developed PVP/PEG/pullulan-DCPD composites demonstrated promising physicochemical and biological properties and may serve as preliminary bone-facing materials for future osteochondral tissue engineering applications. Further studies are required to investigate their osteogenic potential and long-term biological performance.

Keywords: Biomaterial, polymer-ceramic composite, pullulan, osteochondral regeneration.

***Address for correspondence**: Karina Niziołek, Cracow University of Technology, CUT Doctoral School, Faculty of Materials Engineering and Physics, Department of Materials Science, 37 Jana Pawła II Av., 31-864 Krakow, Poland; Cracow University of Technology, Faculty of Materials Engineering and Physics, Department of Materials Science, 37 Jana Pawła II Av., 31-864 Krakow, Poland. E-mail: karina.niziolek@pk.edu.pl.

Copyright policy: © 2026 The Author(s). Published by Forum Multimedia Publishing, LLC. This article is distributed in accordance with Creative Commons Attribution Licence (http://creativecommons.org/licenses/by/4.0/).

Introduction

Osteochondral defects, involving damage to both articular cartilage and the underlying subchondral bone, represent a significant clinical and socioeconomic challenge. These injuries may arise from trauma, degenerative diseases such as osteoarthritis, or repetitive mechanical loading, and are characterised by a limited intrinsic healing capacity, particularly in cartilage tissue [1,2]. It is estimated that cartilage-related lesions affect millions of patients worldwide, with osteoarthritis being one of the leading causes of disability globally. In parallel, the growing clinical demand for effective treatment strategies is reflected in the rapid expansion of the cartilage repair market. The global cartilage repair and regeneration market is estimated to reach nearly USD 2 billion in 2026 and is expected to grow to approximately USD 3.7 billion by 2031, with a high annual growth rate exceeding 13%. Similarly, the knee cartilage repair segment alone is projected to reach over USD 2.6 billion by 2031, driven by the increasing incidence of osteoarthritis, sports injuries, and ageing populations [3]. This dynamic growth highlights not only the scale of the clinical problem but also the urgent need for

advanced biomaterials capable of supporting effective tissue regeneration. The complexity of osteochondral tissue, composed of a soft, viscoelastic cartilage layer and a stiff, mineralized bone phase, makes its regeneration particularly challenging [4,5]. Successful repair requires the simultaneous restoration of both tissue types, as well as the recreation of their functional interface, which plays a critical role in load transfer and joint mechanics.

Despite significant advances in clinical treatment strategies, the effective regeneration of osteochondral defects remains challenging. Conventional approaches, such as microfracture, autologous chondrocyte implantation, and osteochondral grafting, are widely used in clinical practice; however, they are often associated with several limitations [6,7]. In particular, these methods frequently lead to the formation of fibrocartilage rather than native hyaline cartilage, which exhibits inferior mechanical properties and reduced durability [8,9]. Additionally, insufficient integration between regenerated cartilage and subchondral bone, as well as donor-site morbidity and limited graft availability, further limit the long-term success of these treatments [10]. As a result, there is a growing need for alternative strategies that enable the restoration of both cartilage and bone tissue in a controlled and functionally integrated manner.

In response to these limitations, biomaterial-based approaches have emerged as a promising strategy for osteochondral tissue regeneration. In particular, hydrogel systems have gained considerable attention due to their structural similarity to the native extracellular matrix (ECM), high water content, and tunable physicochemical properties [11,12]. These characteristics enable hydrogels to provide a supportive microenvironment for cell adhesion, proliferation, and differentiation. Moreover, their injectability and ability to fill irregular defect sites make them especially attractive for minimally invasive therapies. However, despite these advantages, conventional hydrogel systems often exhibit significant drawbacks that limit their application in osteochondral regeneration. In particular, many hydrogels lack sufficient mechanical strength and structural stability required for load-bearing environments, as well as bioactive cues necessary to stimulate tissue-specific cellular responses [13,14]. As a result, purely polymeric hydrogels are frequently unable to support the simultaneous regeneration of both cartilage and subchondral bone, highlighting the need for the development of more advanced, multifunctional systems [15].

To overcome the limitations of conventional hydrogels, increasing attention has been directed toward hybrid systems combining synthetic polymers with naturally derived polysaccharides [16,17]. Synthetic polymers, such as poly(ethylene glycol) (PEG) and poly(vinylpyrrolidone) (PVP), are widely used due to their well-defined structure, reproducibility, and tunable physicochemical properties [18]. PEG is particularly valued for its high hydrophilicity and flexibility, which promote water uptake and facilitate the formation of hydrated networks, while PVP contributes to improved structural stability and mechanical strength due to its more rigid molecular structure [19,20]. In parallel, natural polysaccharides, such as pullulan, have been introduced to enhance the biological performance of hydrogel systems. Pullulan is a non-toxic and biodegradable polysaccharide characterised by excellent film-forming ability and high water solubility, which can support cell-material interactions and improve the overall biofunctionality of the system [16,21]. The combination of synthetic and natural components enables the design of hybrid hydrogels with tailored properties, allowing for fine-tuning of mechanical behaviour, swelling characteristics, and biological response. Nevertheless, despite these advantages, polymer-based hydrogels remain largely bioinert and are often unable to actively stimulate tissue regeneration, particularly in the context of osteochondral applications. This limitation highlights the need for the incorporation of additional bioactive components capable of inducing specific cellular responses [13,22].

To address the limitations of bioinert polymer systems, calcium phosphate-based materials have been widely investigated as bioactive components for tissue engineering applications. In particular, dicalcium phosphate dihydrate (DCPD) has attracted increasing interest due to its high solubility and ability to release biologically relevant ions, such as calcium (Ca^{2+}) and phosphate ($PO_4{}^{3-}$), which play a crucial role in bone formation and cellular signalling processes [23,24]. The incorporation of calcium phosphate phases into polymer matrices has been shown to enhance osteoconductivity, promote mineralisation, and improve overall biological performance [25]. Unlike more stable calcium phosphate phases, DCPD exhibits relatively fast dissolution behaviour, which enables dynamic ion exchange with the surrounding environment. This feature is particularly advantageous in the context of osteochondral regeneration, where controlled ion release can stimulate osteoblastic activity in the subchondral bone region, while the polymer matrix provides a supportive environment for cartilage regeneration [26]. Moreover, the presence of inorganic particles within the polymer network may contribute to increased mechanical stability and surface roughness, further enhancing cell-material interactions [27]. However, despite the recognised benefits of calcium phosphate incorporation, the design of polymer-ceramic hydrogels remains challenging. In particular, insufficient control over particle dispersion, network structure, and processing conditions may lead to inhomogeneous materials and unpredictable biological performance. Therefore, a systematic approach linking composition, processing parameters, and final material properties is required to fully exploit the potential of such hybrid systems.

Despite growing interest in polymer-ceramic hydrogel systems, a comprehensive understanding of the relationships between precursor suspension behavior, polymer

composition, network architecture, and biological response remains limited. In particular, insufficient attention has been paid to the role of suspension stability and processing parameters in determining the final distribution of the ceramic phase and its subsequent impact on physicochemical and biological properties. Most previous studies have focused primarily on material composition, while the interaction between the processing process, structure, and function is often overlooked. Therefore, this study aimed to develop and characterize DCPD-reinforced PEG-PVP-pullulan photopolymerizable hydrogels, with a particular emphasis on establishing a direct relationship between material composition, processing conditions, and biological properties. The influence of polymer concentration on ceramic sedimentation and of network structure on swelling behavior, degradation, ion release, surface properties, and biocompatibility was systematically investigated. Importantly, this study proposes a rational strategy for designing hybrid polymer-ceramic hydrogels, in which controlling the stability of the precursor suspension and the interactions between the polymer and the ceramic allows for the customization of material properties and biological responses. By combining synthetic polymers, natural polysaccharides, and bioactive ceramic phases, the developed system aims to create a multifunctional platform for osteochondral tissue engineering.

Materials and Methods

Materials

All reagents used for the synthesis of calcium phosphate powders-namely disodium hydrogen phosphate dihydrate ($Na_2HPO_4 \cdot 2H_2O$, CAS no. 10028-24-7), calcium nitrate tetrahydrate ($Ca(NO_3)_2 \cdot 4H_2O$, CAS no. 13477-34-4), and ammonium hydroxide (NH_4OH, 25%, CAS no. 1336-21-6) were obtained from Sigma-Aldrich (Darmstadt, Germany). PEG (Mw = 10,000, CAS no. 25322-68-3), PVP (Mw = 10,000, CAS no. 9003-39-8), poly(ethylene glycol) diacrylate (PEGDA, Mn = 575 and 700, CAS no. 26570-48-9), and the photoinitiator 2-hydroxy-2-methylpropiophenone (CAS no. 7473-98-5) were purchased from Sigma-Aldrich (Darmstadt, Germany). Pullulan (CAS no. 9057-02-7) was obtained from Angene (Cambridge, UK). Ringer's solution, artificial saliva, and simulated body fluid (SBF) were prepared using analytical grade reagents. Sodium chloride (NaCl, CAS no. 7647-14-5), potassium chloride (KCl, CAS no. 7447-40-7), calcium chloride ($CaCl_2$, CAS no. 10043-52-4), and sodium sulfate (Na_2SO_4, CAS no. 7757-82-6) were purchased from Eurochem BGD (Tarnów, Poland). Disodium hydrogen phosphate ($Na_2HPO_4 \cdot H_2O$, CAS no. 7558-79-4), sodium sulfide ($Na_2S \cdot 9H_2O$, CAS no. 1313-84-4), dipotassium hydrogen phosphate ($K_2HPO_4 \cdot 3H_2O$, CAS no. 16788-57-1), and magnesium chloride hexahydrate ($MgCl_2 \cdot 6H_2O$, CAS no. 7791-18-6) were obtained from Chempur (Piekary Śląskie, Poland). Sodium bicarbonate ($NaHCO_3$, CAS no. 144-55-8) was supplied by DOR-CHEM (Kraków, Poland), while urea (CAS no. 57-13-6) and hydrochloric acid (HCl, 35–38%, CAS no. 7647-01-0) were purchased from Stanlab (Lublin, Poland). Tris(hydroxymethyl)aminomethane (Tris, CAS no. 77-86-1) was obtained from POCH (Gliwice, Poland). Phosphate-buffered saline (PBS, BO0971D) was prepared using commercially available tablets (OXOID, Basingstoke, UK). Demineralised water used for all solutions was obtained using a Hydrolab HLP 5sp system (Wodzisław Śląski, Poland).

MC3T3-E1 Subclone 14 cells (a pre-osteoblastic cell line derived from mouse calvaria) were purchased from Sigma-Aldrich (Darmstadt, Germany). Reagents used for biological assays, including α-Minimum Essential Medium (α-MEM, M8042), fetal bovine serum (FBS, F4135), penicillin–streptomycin solution (P4333), amphotericin B (A2942), L-glutamine (G7513), Dulbecco's phosphate-buffered saline (DPBS, P3813), Triton X-100 (X100), 0.25% trypsin-ethylenediaminetetraacetic acid (EDTA) solution (SM-2003), trypan blue solution (T6146), 37 %vol. formaldehyde solution (CAS no. 50-00-0), 25 %vol. glutaraldehyde (G6257), glacial acetic acid (CAS no. 64-19-7), ethanol 96 %vol. (CAS no. 64-17-5), and Hank's balanced salt (H8264) were purchased from Sigma-Aldrich (Darmstadt, Germany). The 22,3-Bis(2-methoxy-4-nitro-5-sulfophenyl)-2H-tetrazolium-5-carboxanilide inner salt (XTT, X4626) assay reagents, including XTT sodium salt and phenazine methosulfate (PMS, P9625), as well as the neutral red dye used in the neutral red uptake (NRU, N7005) assay, were also obtained from Sigma-Aldrich (Darmstadt, Germany).

Preparation of Ceramic Powder

DCPD was synthesized by wet precipitation using $Ca(NO_3)_2 \cdot 4H_2O$ and $Na_2HPO_4 \cdot 2H_2O$ as precursors for calcium and phosphate, respectively. In brief, the calcium precursor solution was added dropwise ($\approx$ 1 drop$\cdot s^{-1}$) to the phosphate solution under continuous magnetic stirring, while adjusting the pH with 25% ammonium hydroxide (NH_4OH). The reaction was carried out at a target Ca/P molar ratio of 1.0, which promoted the precipitation of brushite. After complete addition, the resulting suspension was left for 24 hours, then the precipitate was collected, washed repeatedly with distilled water until a neutral pH was obtained, and finally freeze-dried to obtain DCPD powder.

The detailed synthesis protocol is described in our previous publication, in which this ceramic powder was designated as "1.0"; in this study, it is referred to as DCPD [28].

Determination of Ceramic Sedimentation Rate

The sedimentation rate of DCPD powder in polymer solutions was measured as previously described [29]. In order to obtain composites, a UV photopolymerisation process lasting 4 minutes was used. To avoid excessive sed-

Table 1. Compositional design and formulation of the polymer-ceramic composites.

Sample	PEG (mL)	PVP (mL)	Pullulan (g)	DCPD (g)	PEGDA (mL)	Photoinitiator (μL)
A	7.5	2.5	0.5	-	2	50
B	5	5				
C	2.5	7.5				
A-DCPD	7.5	2.5		0.5		
B-DCPD	5	5				
C-DCPD	2.5	7.5				

imentation of ceramics in an aqueous polymer solution, the sedimentation rate of DCPD was analysed at different PVP/PEG concentrations. A 1:1 polymer ratio (PVP: PEG) and aqueous concentrations of 0%, 5%, 10%, 15%, 20% and 25%. The analysis was performed using a MultiScan MS20 DataPhysics Instruments device (Filderstadt, Germany). Each measurement was performed over a period of 60 minutes, with 120 scans taken at 12-second intervals.

Preparation of Polymer-Ceramic Composites

Composite biomaterials based on a PVP/PEG polymer matrix containing the polysaccharide pullulan and DCPD were created using photopolymerization. The overall synthesis procedure is schematically illustrated in Fig. 1. Initially, a broader range of polymer and polymer-ceramic formulations was designed and prepared to optimize the composition and processing parameters. The complete formulation matrixes is presented in **Supplementary Table 1**. Based on this preliminary screening, selected formulations were used in the main study. First, a solution of PVP and PEG polymers was prepared at a concentration of 15% (w/v) each. Then, appropriate volumes of these solutions were transferred to beakers according to the composition specified in Table 1. 0.5 g of pullulan was added to each preparation and stirred until completely dissolved. Next, 0.5 g of DCPD powder was gradually added, stirring continuously to ensure homogeneous dispersion of the ceramic phase in the polymer matrix. After homogenization, 2 mL of PEGDA with a molecular weight of Mn 700 was introduced as a cross-linking agent, followed by 50 μL of photoinitiator (2-hydroxy-2-methylpropiofenone). The resulting mixtures were thoroughly mixed, transferred to Petri dishes with a diameter of 9 cm, and irradiated with UV light for 4 minutes using a Medilux UV 436 HF lamp (Medilux, Korntal-Münchingen, Germany) for photopolymerization and formation of a cross-linked hydrogel network.

Fourier Transform Infrared Spectroscopy

Fourier transform infrared spectroscopy (FT-IR) was used to characterize the chemical structure of pure base materials (PVP, PEG, pullulan, DCPD, and PEGDA) and the polymer-ceramic composites produced. The analysis was performed to confirm the presence of characteristic functional groups of individual components and to evaluate potential physicochemical interactions after incubation in media simulating the internal environment of the body. The spectra were collected using a Nicolet iS5 FT-IR spectrometer (Thermo Scientific, Loughborough, UK) equipped with an iD7 ATR accessory . The measurements were performed in the range of 4000–400 cm^{-1} with 32 scans per sample at a spectral resolution of 4.0 cm^{-1}, at room temperature.

Incubation Studies

Fluid Preparation

In vitro incubation studies were conducted to evaluate the physicochemical stability and potential bioactivity of the developed composites under conditions simulating selected physiological environments. For this purpose, four incubation fluids were used: distilled water, Ringer's solution, artificial saliva, and SBF.

Distilled water was used without further modification. Ringer's solution, artificial saliva, and SBF were prepared according to the compositions listed in Table 2, Table 3, and Table 4. The reagents were added sequentially under constant stirring, ensuring complete dissolution of each component prior to the addition of the next.

Ringer's solution and artificial saliva were prepared at room temperature. The pH of Ringer's solution was in the range of 6.4–6.5, whereas the pH of artificial saliva was 5.5. For SBF preparation, 700 mL of distilled water was heated to 36.5 °C (± 0.5 °C), and the reagents were added successively under continuous stirring. The pH was adjusted to 7.40–7.45 using HCl and Tris, and the final volume was adjusted to 1000 mL with distilled water. All incubation fluids were freshly prepared prior to use.

Table 2. Chemical composition of the Ringer's solution formulation.

Sequence	Reagent	Amount ($g \cdot L^{-1}$)
1	NaCl	8.600
2	KCl	0.300
3	$CaCl_2 \cdot 2H_2O$	0.480

Potentiometric and Conductometric Measurements

To evaluate the behaviour of the developed materials under conditions simulating physiological environments, incubation studies were performed in four media: SBF, Ringer's solution, artificial saliva, and distilled water. Each

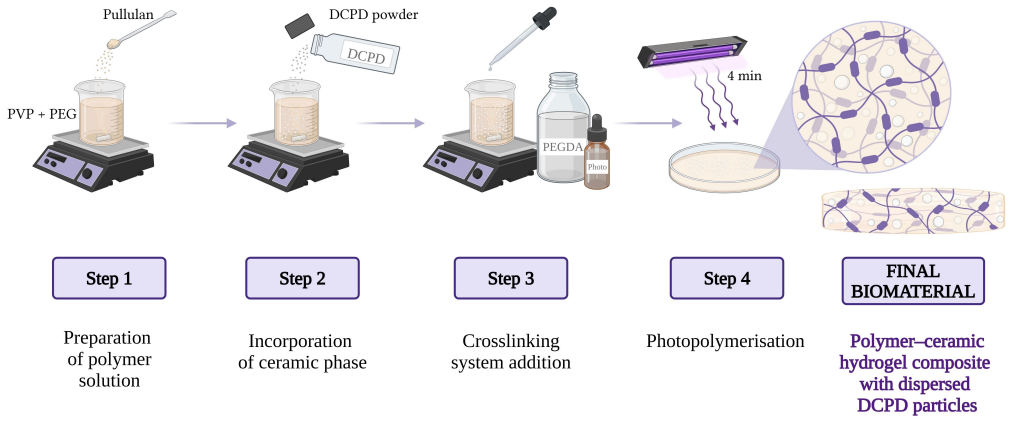

Fig. 1. Schematic illustration of the preparation of polymer-ceramic hydrogels based on a PVP/PEG matrix containing pullulan and DCPD. Created in BioRender. L. (2026) https://BioRender.com/fcoueqj.

Table 3. Chemical composition of the artificial saliva formulation.

Sequence	Reagent	Amount ($g \cdot L^{-1}$)
1	NaCl	0.400
2	KCl	0.400
3	$CaCl_2 \cdot 2H_2O$	0.795
4	$Na_2HPO_4 \cdot H_2O$	0.780
5	$Na_2S \cdot 9H_2O$	0.005
6	$CO(NH_2)_2$	1.000

Table 4. Chemical composition of the SBF formulation.

Sequence	Reagent	Amount ($g \cdot L^{-1}$)
1	NaCl	8.035
2	$NaHCO_3$	0.355
3	KCl	0.225
4	$K_2HPO_4 \cdot 3H_2O$	0.231
5	$MgCl_2 \cdot 6H_2O$	0.311
6	1M HCl	39 mL
7	$CaCl_2$	0.292
8	Na_2SO_4	0.072
9	Tris	6.118
10	1M HCl	Appropriate amount for pH adjustment

sample was immersed in 100 mL of the respective medium in airtight, sterile containers. The samples were incubated at 36.6 °C in a POL-EKO ST 5 B SMART incubator (POL-EKO, Wodzisław Śląski, Poland). For each formulation, three independent replicates were prepared and analysed.

The pH and ionic conductivity of the incubation media were measured after 1, 3, 7, 10, and 14 days using an Elmetron CX-701 multifunction meter (Elmetron, Zabrze, Poland) equipped with an EPS-1 pH electrode and an ECF-1 conductivity probe (Elmetron, Zabrze, Poland). All measurements were performed at room temperature.

Determination of Swelling Capacity

The swelling capacity of materials, which involves the absorption of liquids into the polymer structure, is defined as one of the strategies for assessing the potential of materials for use as carriers of active substances. This parameter is influenced by the composition of the materials and the type of liquid itself.

Composite samples weighing 0.1 g were prepared and immersed in 100 mL of distilled water, kept in sterile, sealed containers at a temperature of 36.6 °C. The samples were then weighed after 30 minutes, 1 hour, 3 hours, 1 day, 3 days, 7 days, 10 days, or 14 days. In order to measure the weight during the analysis, the samples were removed from the solutions and gently drained using filter paper. The swelling capacity of the samples was determined according to equation (Eqn. 1), where m_0 is the dry weight of the sample and m_1 is the weight of the sample at a specific incubation time:

$$Swelling\ ability = \frac{m_1 - m_0}{m_0} \times 100\% \quad (1)$$

Using Voigt's viscoelastic model (Eqn. 2), the swelling kinetics were determined by defining equilibrium swelling and the rate parameter τ. In the equation, S_e means equilibrium swelling (%), S_t means swelling over time t (%), t means time (min), and τ means the rate parameter indicating the time needed for the sample to absorb 0.63 of its maximum swelling (min) [30].

$$S_t = S_e \left[1 - e^{-\frac{t}{\tau}}\right] \quad (2)$$

Degradation Studies

The degradation behaviour of the developed polymer-ceramic composites was evaluated under simulated physiological conditions. Disc-shaped samples with an initial dry mass of approximately 0.1 g were placed in sterile, sealed containers containing 100 mL of the selected incubation media: SBF, PBS, artificial saliva, Ringer's solution, and distilled water (reference).

PBS was prepared by dissolving one tablet in 100 mL of distilled water. All samples were incubated at 36.6 °C for 14 days in a POL-EKO ST 5 B SMART incubator (POL-EKO, Wodzisław Śląski, Poland). The containers remained sealed throughout the incubation period. Three independent replicates were prepared for each material formulation.

After 14 days, the samples were removed from the incubation media, dried to constant mass, and weighed. The degree of degradation was calculated using the following equation (Eqn. 3):

$$Degree\ of\ degradation\ = \frac{m_{t_0} - m_t}{m_{t_0}} \times 100\% \quad (3)$$

where m_{t_0} is the initial dry mass of the sample (g), and m_t is the dry mass after the incubation period (g).

Scanning Electron Microscopy (SEM) With Elemental Composition Analysis

The morphology of the composite surfaces was examined using SEM. For this purpose, a JEOL IT200 microscope (JEOL Ltd, MA, USA) was used. The analysis was carried out to assess the effect of the composition of the materials on their morphology. Prior to SEM measurements, the samples were coated with a gold nanolayer using a DII-29030SCTR Smart Coater (JEOL Ltd, MA, USA). The microscope was equipped with an energy-dispersive X-ray spectroscopy (EDS) detector, which was used to perform elemental analysis of the sample surfaces. Elemental analysis was carried out by determining the mass percentage (%M.) and atomic percentage (%At.). The measurements were performed at ×500 magnification.

Surface Roughness Analysis

Surface morphology and quantitative roughness measurements were carried out using a VHX Series digital microscope (Keyence, Osaka, Japan). Images were captured in 4K resolution (4000 × 3000 pixels), with magnifications ranging from 500× to 2500×. The high-dynamic-range (HDR) imaging mode was applied to enhance surface detail. Three-dimensional surface mapping and profile analysis were performed using the VHZ-7000 series 4K CMOS optical system (Keyence, Osaka, Japan), enabling precise topographical characterisation.

Surface roughness was evaluated based on 3D measurements, and the parameters Ra and Rz were determined. The Ra value (arithmetical mean roughness) reflects the average deviation of the surface profile from the mean line, providing general information about surface irregularities. The Rz parameter represents the average maximum height difference between the highest peak and the deepest valley within the sampling length, characterising extreme surface features.

Hardness Measurement

The hardness of the samples was determined on the Shore D (HD) scale in order to assess the effect of the composition and the addition of DCPD on the mechanical properties of the materials. A Sauter HDD 100-1 hardness tester (KERN & SOHN GmbH, Balingen, Germany) was used for this purpose, and the test samples were 4 mm thick.

Sterilisation and Sample Preparation for Biological Studies

Samples intended for biological evaluation were prepared according to the procedure described in subsection "Preparation of Polymer-Ceramic Composites". Briefly, the polymer-ceramic mixture was prepared as previously described, and aliquots of 0.5 mL were dispensed into the wells of a 24-well culture plate. The formulations were then subjected to UV-induced photopolymerisation under the same conditions as described earlier, resulting in the formation of crosslinked hydrogel specimens directly within the wells.

Before conducting biological assays, all composite samples were sterilised by exposure to gamma radiation at a dose of 35 kGy. Irradiation was performed using a ^{60}Co gamma source at the Institute of Applied Radiation Chemistry, Lodz University of Technology (Łódź, Poland).

In Vitro Biological Evaluation

Cell Culture Conditions

MC3T3-E1 Subclone 14 cells, a mouse preosteoblast cell line commonly used as a model for studying osteoblast differentiation and bone tissue formation, were cultured in α-MEM supplemented with 10% (v/v) FBS, 2.5 mM glutamine, and antibiotics, including penicillin (10 μg·mL^{-1}), streptomycin (100 μg·mL^{-1}), and amphotericin (0.625 μg·mL^{-1}). The cells were maintained at 37 °C in a humid atmosphere with 5% CO_2. The cultures were passaged every 2–3 days and maintained until approximately 85–90% confluence was reached.

Indirect Cytotoxicity Tests

The indirect cytotoxicity of the developed materials was assessed using extract-based tests in accordance with ISO 10993-5 and ISO 10993-12 [31,32]. MC3T3-E1 Subclone 14 cells were seeded into 96-well plates at a density of 2×10^4 cells per well in 200 μL of α-MEM culture medium and incubated for 24 hours at 37 °C in a humid atmosphere containing 5% CO_2. Concurrently, extracts were prepared

from the test materials by incubating 30 mg of each sample in 1 mL of α-MEM medium for 24 hours at 37 °C under standard culture conditions (5% CO_2). A slight adjustment to the amount of material used for extract preparation (30 mg·mL^{-1}) was necessary due to the material's swelling ability. The possibility of modifying this proportion is permitted under ISO 10993-12 [32]. After incubation, the extracts were collected and used for cytotoxicity assessment. After the initial cell culture period, the medium was removed and replaced with 200 μL of the prepared extracts. Cells cultured in standard medium served as a negative control, while cells treated with 0.1% (v/v) Triton X-100 (15 minutes of exposure, followed by DPBS washing) were used as a positive control. The cells were then incubated with the extracts. Cytotoxicity was assessed after 24 hours (day 1) and 48 hours (day 2) of exposure to the extracts. For each time point, the tests were conducted independently under identical conditions. All experiments were performed in six replicates (n = 6).

NRU assay was performed to assess the lysosomal activity of live cells, based on the ability of metabolically active cells to incorporate and retain neutral red dye in lysosomes. The assay was conducted in accordance with the recommendations of ISO 10993-5 [31]. A neutral red stock solution was prepared at a concentration of 4 mg·mL^{-1} in PBS, filtered prior to use, and then diluted in culture medium to obtain a working solution with a final concentration of 40 μg·mL^{-1}. After 24 and 48 hours of exposure of MC3T3-E1 cells to material extracts, the extracts were removed from the wells. Subsequently, 200 μL of the neutral red working solution was added to each well. The plates were incubated for 3 hours at 37 °C in a humid atmosphere containing 5% CO_2 to allow dye uptake into the lysosomes. After incubation, the dye solution was removed, and the cells were gently washed twice with PBS (200 μL per well) to remove excess dye. The cells were then fixed by adding 150 μL of a 5% glutaraldehyde solution in PBS and incubating for 5 minutes. After removing the fixative, the absorbed dye was extracted by adding 200 μL of a destain solution consisting of 50% ethanol, 49% deionized water, and 1% glacial acetic acid. The plates were placed on an orbital shaker 15 minutes before the 4-hour mark to ensure complete dissolution of the dye. Absorbance was measured at 540 nm with a reference wavelength of 660 nm using a microplate reader (BioTek 800 TS, BioTek Instruments, MA, USA).

Cell viability was calculated according to the following equation (Eqn. 4):

$$\%\, Cell\ viability = \frac{(A_{540} - A_{660})_{sample}}{(A_{540} - A_{660})_{control}} \times 100\% \quad (4)$$

Cells treated with 0.1% (v/v) Triton X-100 served as the positive control. All measurements were performed in six replicates (n = 6), and the experiments were conducted independently after 24 h and 48 h of exposure to the extracts.

To perform the XTT reduction assay, a fresh XTT working solution was prepared by dissolving XTT at a concentration of 1 mg·mL^{-1} in a sterile Hank's balanced salt solution. PMS was then added as an electron-coupling reagent at a concentration of 5 μL·mL^{-1} from a 5 mM stock solution. After 24 and 48 hours of exposure of MC3T3-E1 cells to material extracts, the culture medium was removed and replaced with 100 μL of XTT working solution in each well. The plates were incubated at 37 °C for 4 hours in a humidified atmosphere containing 5% CO_2. After incubation, absorbance (A) was measured at 450 nm with a reference wavelength of 630 nm using a microplate reader (BioTek 800 TS, BioTek Instruments, MA, USA).

Cell viability was calculated according to the following equation (Eqn. 5):

$$\%\, Cell\ viability = \frac{(A_{450} - A_{630})_{sample}}{(A_{450} - A_{630})_{control}} \times 100\% \quad (5)$$

Cells cultured in standard medium served as the negative control, while cells treated with 0.1% (v/v) Triton X-100 served as the positive control. All measurements were performed in six replicates (n = 6), and the experiments were conducted independently after 24 h and 48 h of exposure to the extracts.

Direct Cytotoxicity Tests

Direct cytotoxicity of the investigated materials was evaluated using MC3T3-E1 cells and the XTT assay. The samples were positioned centrally in 24-well plates and immobilized with a thin layer of agar. The agar served as a non-adhesive substrate, preventing cell attachment to the well surface and ensuring that cells adhered exclusively to the material, thereby avoiding artificially elevated viability results [33]. MC3T3-E1 cells were seeded directly onto the samples at a density of 1×10^5 cells per well. After 1 h to allow cell attachment, culture medium was added to a final volume of 1 mL per well. The cells were then cultured under standard conditions (37 °C, 5% CO_2) for 48 h.

Control cells (positive and negative controls) were cultured on polystyrene (PS) wells under identical conditions. After incubation, a positive control was prepared by treating selected wells with 0.1% (v/v) Triton X-100 for 15 min, followed by rinsing with DPBS. Wells containing cells cultured in medium only served as the negative control. After the incubation period, the culture medium was removed and replaced with a working XTT solution, prepared by dissolving XTT (1 mg·mL^{-1}) in a sterile Hank's balanced salt solution supplemented with PMS at a concentration of 5 μL·mL^{-1} (from a stock solution of 5 mM). 300 μL of the XTT solution was added to each well. The plates were in-

cubated for 4 hours at 37 °C in a humidified atmosphere containing 5% CO_2. After incubation, 100 μL of the supernatant was transferred to a 96-well plate, and absorbance was measured at 450 nm with a reference wavelength of 630 nm using a BioTek 800 TS microplate reader (BioTek Instruments, MA, USA). Cell viability was expressed as a percentage relative to the negative control (cells cultured in PS medium), which was defined as 100%. All measurements were performed in six replicates (n = 6).

Direct Proliferation Tests

Cell proliferation on the test materials was assessed using the XTT assay. Sample preparation and seeding into 24-well plates were performed as described in the section on direct cytotoxicity assays. MC3T3-E1 cells were seeded onto the sample surfaces at a density of 3×10^4 cells per well, followed by medium addition to a final volume of 1 mL per well. Cultures were maintained under standard conditions (37 °C, 5% CO_2). Cell proliferation was assessed after 1, 3, and 7 days of culture. At each time point, the culture medium was removed and replaced with XTT working solution, prepared as described above. 300 μL of XTT solution was added to each well, and the plates were incubated for 4 hours at 37 °C in a humidified atmosphere containing 5% CO_2. After incubation, 100 μL of the supernatant was transferred to a 96-well plate, and absorbance was measured at 450 nm with a reference wavelength of 630 nm using a BioTek 800 TS microplate reader (BioTek Instruments, MA, USA). To quantitatively determine cell counts under identical experimental conditions, a calibration curve correlating absorbance with cell count was prepared. Based on this calibration, the absorbance values obtained for the samples were converted to cell counts. All experiments were performed in six replicates (n = 6).

Cell Morphology Evaluation

To evaluate early cell attachment and morphology, SEM observations were performed after 24 h of culture. Additional analyses were carried out following the direct cytotoxicity assay and after 7 days of culture during the direct proliferation study. In all cases, the samples were prepared for morphological evaluation of cell attachment on the surface of the developed polymer-ceramic hydrogels. The culture medium was removed, and the specimens were gently rinsed with PBS to remove non-adherent cells and residual medium components. The adherent cells were then fixed using a 4% (v/v) formaldehyde solution.

Subsequently, the samples were dehydrated through a graded ethanol series with increasing concentrations of 35%, 50%, 70%, and 90%, with each step lasting 15 min. The dehydration procedure was completed by two additional immersions in 96% ethanol. After drying, the morphology and distribution of MC3T3-E1 cells on the material surfaces were examined using SEM with a JEOL IT200 microscope (JEOL Ltd., Tokyo, Japan). Prior to imaging, the samples were sputter-coated with a thin gold layer using a DII-29030SCTR Smart Coater (JEOL Ltd., MA, USA).

Statistical Analysis

Statistical analysis was performed using one-way analysis of variance (ANOVA) to determine significant differences between the analysed datasets. For cell proliferation studies, a two-way ANOVA was additionally performed, considering material composition and incubation time as independent factors, followed by Tukey's post hoc test for multiple comparisons. The level of statistical significance was defined as $*p < 0.05$, $**p < 0.01$, and $***p < 0.001$. All calculations were carried out using OriginPro 2026 software (OriginLab Corporation, MA, USA).

Results

Determination of Ceramic Sedimentation Rate

In order to determine the optimal concentration of the PVP/PEG solution in which the DCPD powder was suspended, a sedimentation rate analysis was performed. Changes in the position of the sedimentation front as a function of time are presented in Fig. 2, while the calculated sedimentation rates are summarised in Table 5.

Based on the results obtained, a correlation was observed between the polymer concentration and the stability of the suspension. In the case of a mixture containing only distilled water (0%), the fastest sedimentation of DCPD particles was observed, indicating low stability of the mixture. The sedimentation rate determined for this sample is -6.93 ± 0.23 mm·min^{-1}. As the concentration of PVP/PEG increases, the sedimentation process gradually slows down, and the sedimentation rate values decrease to -2.29 ± 0.04 mm·min^{-1} for the solution with the highest concentration, which is 25%. The graph demonstrates a shift of the sedimentation curves towards longer times with increasing polymer content. This phenomenon can be associated with an increase in the viscosity of polymer solutions, which limits the mobility of DCPD particles in suspension and, as a consequence, slows down their settling under the influence of gravity. Although the highest suspension stability was obtained for polymer concentrations of 20% and 25%, these polymers were difficult to dissolve and required additional heating of the mixture. For this reason, a concentration of 15% was considered the most favourable. For this composition, relatively slow particle sedimentation of -2.97 ± 0.06 mm·min^{-1} was observed, while maintaining good suspension homogeneity and adequate processability. Thus, a 15% PVP/PEG solution was selected for further stages of composite preparation.

Physicochemical Characterisation

The FT-IR spectra of the individual pure components and the resulting polymer-ceramic composites are shown in Fig. 3. The PEG spectrum exhibited characteristic bands in the range of approximately 2950–2880 cm^{-1}, correspond-

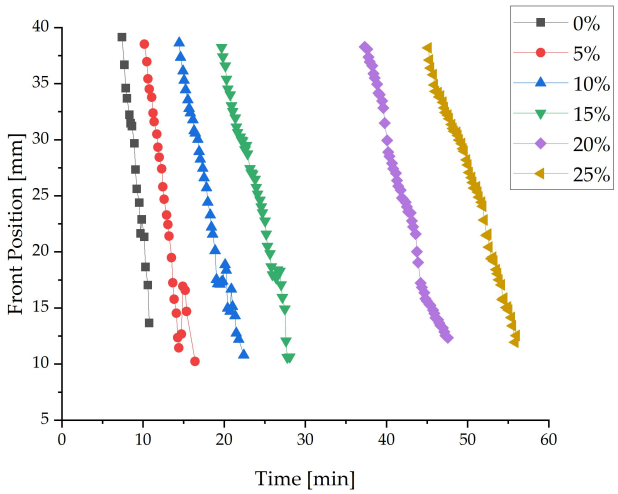

Fig. 2. Migration front position of DCPD powder in PVP/PEG solutions of different concentrations as a function of time.

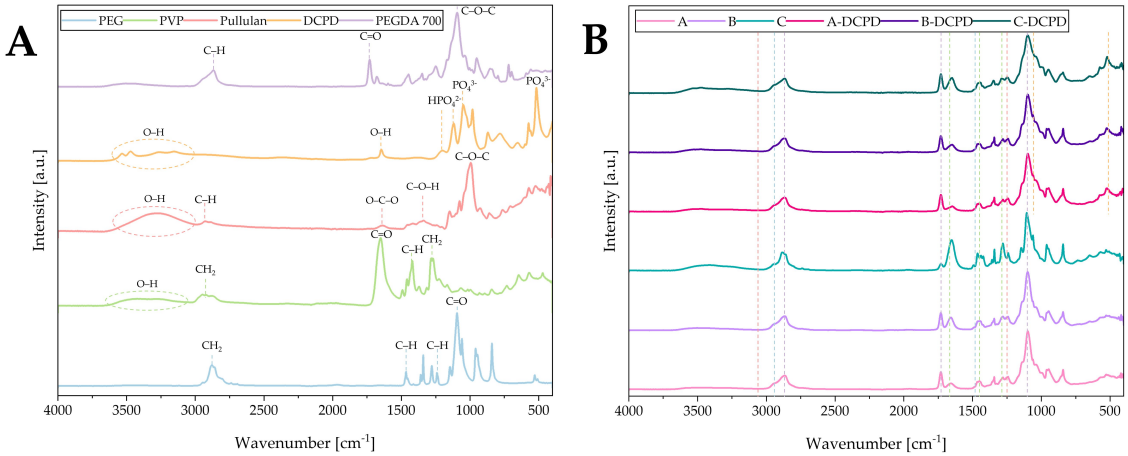

Fig. 3. FT-IR spectra of materials and composites. (**A**) The individual components (PEG, PVP, pullulan, DCPD, and PEGDA). (**B**) The obtained polymer and polymer-ceramic composites.

Table 5. Sedimentation rate of DCPD powder in PVP/PEG solutions of different concentrations.

No.	PVP: PEG (%)	Sedimentation rate (mm·min^{-1})
1	0	–6.93 ± 0.23
2	5	–4.99 ± 0.27
3	10	–3.54 ± 0.10
4	15	–2.97 ± 0.06
5	20	–2.75 ± 0.05
6	25	–2.29 ± 0.04

ing to the stretching vibrations of C–H bonds, and a strong band in the region of 1100 cm^{-1}, attributed to stretching vibrations of C–O–C bonds in ether groups [34–36]. In the case of PVP, a distinct band was observed at approximately 1650 cm^{-1}, corresponding to the carbonyl group (C=O) of the lactam ring, along with bands in the 1450–1280 cm^{-1} range attributed to C–N stretching vibrations [37–39]. The pullulan spectrum showed a broad band in the 3500–3200 cm^{-1} range associated with O–H stretching vibrations, indicating its hydrophilic nature, as well as strong bands in the 1100–1000 cm^{-1} range corresponding to C–O and C–O–C vibrations characteristic of polysaccharides [40–42]. In the case of dihydrate DCPD, characteristic phosphate-related bands were observed in the 600–500 cm^{-1} and 1100–1000 cm^{-1} regions, corresponding to PO_4^{3-} vibrations, while the band near 1640 cm^{-1} was associated with water molecules present in the crystal structure [28]. The PEGDA spectrum exhibited a band at approximately 1720 cm^{-1} attributed to the ester carbonyl groups (C=O), as well as signals near 1630 cm^{-1} corresponding to the C=C stretching vibrations of the acrylate groups [43].

The FT-IR spectra of the composites (A–C and A–

C-DCPD) confirmed the presence of characteristic bands of the polymer matrix components. A broad absorption band at 3500–3200 cm^{-1} and a band at ~1100 cm^{-1} indicate the presence of –OH and C–O–C groups originating from PEG and pullulan. A band observed at ~1720 cm^{-1} corresponds to the C=O groups of PEGDA. Subsequently, the decrease in band intensity associated with C=C bonds suggests successful photopolymerization and the formation of a cross-linked network. In the case of samples containing DCPD (A-DCPD, B-DCPD, and C-DCPD), additional bands characteristic of PO_4^{3-} were clearly visible at the wavelengths of 600–500 cm^{-1} and 1100–1000 cm^{-1}, confirming the successful incorporation of the ceramic phase into the polymer matrix. Slight shifts and broadening of the bands, particularly in the hydroxyl region, indicate possible intermolecular interactions, such as hydrogen bonds between the polymer chains and the ceramic phase.

The FT-IR spectra of the composite samples after incubation are presented in **Supplementary Fig. 5**. First, the samples containing DCPD retained the characteristic bands of both the polymer matrix and the ceramic phase, indicating that the overall chemical structure of the composites remained intact. However, slight changes in the intensity and sharpness of the phosphate bands were observed, suggesting partial dissolution or surface transformation of the DCPD phase during incubation [44]. Furthermore, after incubation, a noticeable broadening of the O–H band in the 3500–3200 cm^{-1} was observed, which can be attributed to increased hydration of the materials and interactions with the surrounding environment. Slight changes were also detected in the 1700–1600 cm^{-1} region, likely due to the presence of absorbed water or interactions between the polymer matrix and ions in the incubation fluids. In some cases, slight shifts in the PO_4^{3-} bands were observed, suggesting ion exchange processes and structural rearrangements at the surface of the ceramic phase. These changes are consistent with interactions between DCPD and ions present during the incubation.

Swelling Capacity, Swelling and Degradation Behaviour

To evaluate the properties of the obtained hydrogel materials, time-dependent swelling tests were conducted. Changes in the swelling capacity of the tested materials are shown in Fig. 4**A** for polymeric matrices and Fig. 4**B** for composites, while Table 6 summarizes the values of equilibrium swelling (S_e) and the kinetic parameter τ.

Based on the obtained results, all samples exhibit a similar swelling kinetics profile. In the initial stage, a rapid increase in swelling capacity is observed, particularly during the first hours of contact with the medium. Subsequently, the swelling rate slows down significantly, and after approximately 24 hours, the material reaches a state close to swelling equilibrium. This behaviour is characteristic of hydrophilic polymer networks, in which initial swelling is associated with rapid liquid penetration into the most accessible areas of the structure, while further swelling results from a slower reorganisation and loosening of the polymer network.

In the case of polymer matrices without the addition of a mineral phase, the highest S_e was observed for sample A, while the lowest was for sample C. The observed trend indicates that increasing the PEG content of the material enhances its swelling capacity. This phenomenon can be explained by the chemical structure of PEG, whose chains contain numerous oxygen atoms that can form hydrogen bonds with water molecules. Additionally, PEG is characterized by high polymer chain flexibility, which facilitates medium penetration and network expansion [45]. In contrast, a higher PVP content can lead to a more compact structure due to the presence of a pyrrolidone ring in the repeating unit, which limits the ability of liquids to penetrate the material's interior [46].

The addition of DCPD reduced the swelling values of all samples. This effect is due to the presence of the ceramic, which restricts the mobility of the polymer chains and reduces the amount of free space in the polymer network. As a result, the penetration of the medium into the material is impeded, leading to a reduction in the composite's maximum swelling capacity. The addition of DCPD also affected the kinetics of the swelling process. The values of the τ parameter for the composites were higher than those for the corresponding polymer matrices, indicating a slower sorption process, which can be explained by a more complex path of liquid diffusion within the material. The presence of DCPD particles increases the medium's transport path and restricts the freedom of movement of polymer chains, resulting in a slower attainment of equilibrium. Within the composite series, the B-DCPD sample exhibited the highest S_e, while the C-DCPD sample exhibited the lowest. This may suggest that a balanced ratio of PEG and PVP promotes the most favorable composite structure. The S_e and rate parameter (τ) obtained for the additional formulations evaluated during the preliminary screening, including systems crosslinked with PEGDA 575, are presented in **Supplementary Table 2**. These data show trends consistent with those observed for the selected formulations.

Changes in the pH values of the incubation media during exposure to the tested materials are shown in Fig. 5. Overall, the pH values exhibited only moderate fluctuations during the incubation period, indicating the relatively good chemical stability of the developed materials in the tested environments.

In Ringer's solution (Fig. 5**A**), a gradual increase in pH was observed in most samples during the incubation period. Initial values ranged from approximately 6.3 to 6.8 and rose slightly over time, reaching levels close to neutral (approximately 7.0–7.2). This behavior suggests mild interactions between the materials and their surrounding environment, likely related to ion exchange processes occurring at the material-solution interface. A similar trend was ob-

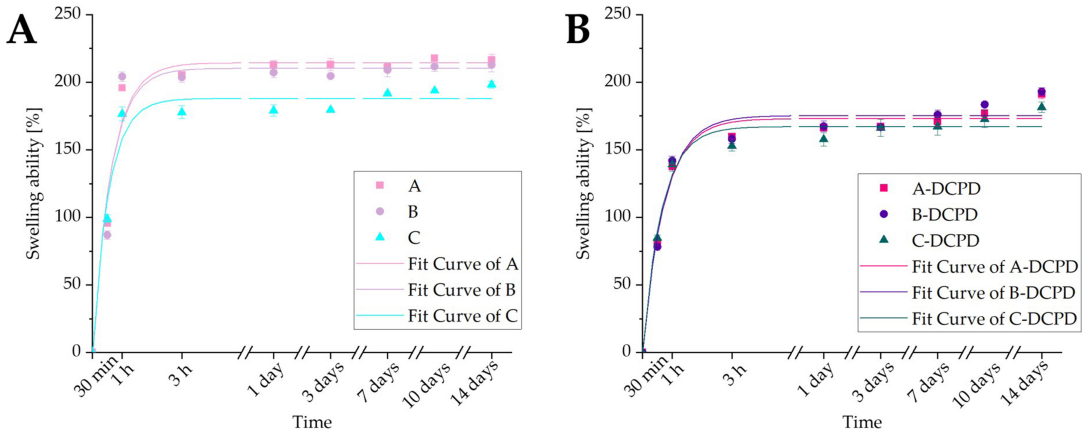

Fig. 4. Swelling kinetics of (A) polymer matrices, (B) composites in distilled water. Data are presented as mean ± SD (n = 3). Solid lines indicate fitted curves describing the swelling behaviour of the individual samples.

Table 6. τ and S_e of polymer matrices and composites.

Sample	S_e (%)	τ
A	216.29 ± 5.65	25.82 ± 3.91
B	208.16 ± 7.41	24.73 ± 5.10
C	188.47 ± 5.08	22.17 ± 3.59
A-DCPD	174.72 ± 3.86	29.66 ± 3.83
B-DCPD	180.45 ± 6.26	26.55 ± 5.33
C-DCPD	169.51 ± 4.63	24.06 ± 3.58

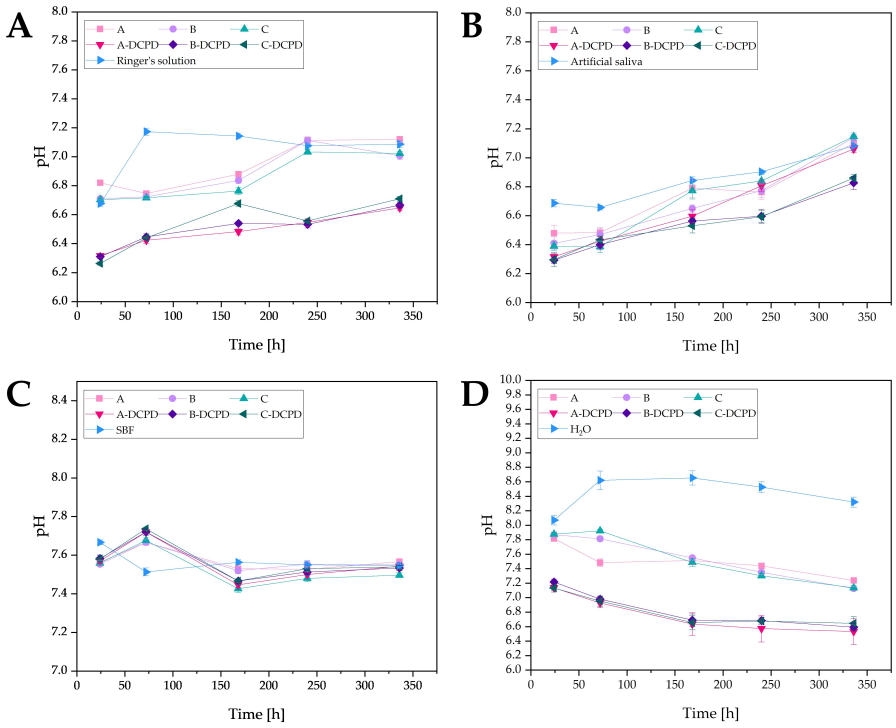

Fig. 5. Time-dependent changes in pH of the incubation media in the presence of the investigated materials. (**A**) Ringer's solution, (**B**) artificial saliva, (**C**) simulated body fluid (SBF), and (**D**) distilled water. Data are presented as mean ± SD (n = 3).

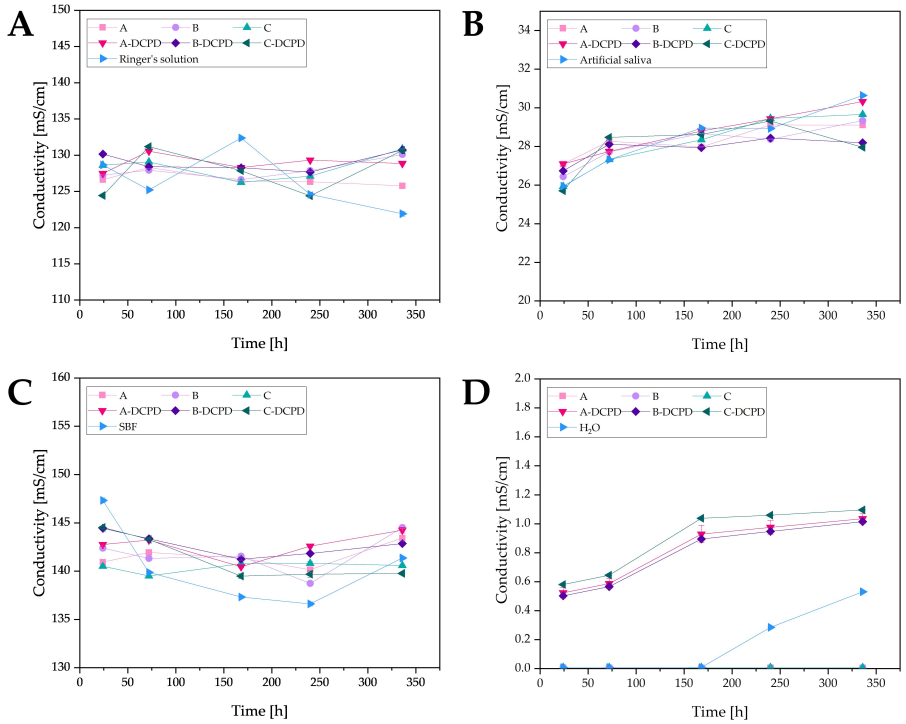

Fig. 6. Changes in ionic conductivity of the incubation media during incubation of the investigated materials. (**A**) Ringer's solution, (**B**) artificial saliva, (**C**) simulated body fluid (SBF), and (**D**) distilled water. Data are presented as mean ± SD (n = 3).

served in artificial saliva (Fig. 5**B**), where pH values also increased slightly during incubation. Initial values in the range of approximately 6.3–6.5 gradually increased to approximately 7.0–7.1 after a longer incubation period. Importantly, the inclusion of the ceramic phase (DCPD) did not cause significant changes in the pH of the environment, indicating that the presence of the calcium phosphate component did not significantly affect the solution's buffering capacity. In the case of SBF (Fig. 5**C**), the pH remained relatively stable throughout the incubation period. These values fluctuated only slightly within the range of approximately 7.4–7.7, suggesting that the tested materials did not significantly disrupt the ionic balance of this physiologically relevant solution. More pronounced fluctuations were observed in distilled water (Fig. 5**D**). In this environment, the pH initially rose and then gradually decreased over time for most samples. This behaviour may be related to ion release processes and the gradual establishment of equilibrium between the material's surface and the surrounding aqueous environment.

To complement the pH analysis, the ionic conductivity of the incubation media was also monitored (Fig. 6). Conductivity measurements provide insight into the extent of ion exchange between the materials and the surrounding fluids.

In Ringer's solution (Fig. 6**A**), conductivity values remained relatively stable throughout the incubation period, with only slight fluctuations observed. This indicates that the materials did not significantly affect the ionic composition of this solution. In artificial saliva (Fig. 6**B**), a slight increase in conductivity was observed during incubation. Conductivity gradually increased from approximately 26–27 $mS \cdot cm^{-1}$ at the start of the experiment to approximately 29–30 $mS \cdot cm^{-1}$ after prolonged exposure, suggesting a slow release of ions from the materials into the surrounding environment. Similarly, in SBF (Fig. 6**C**), conductivity values remained relatively stable, showing only slight changes during the experiment. This behavior further indicates limited interaction between the tested materials and the SBF. A more pronounced change in conductivity was observed in distilled water (Fig. 6**D**). Due to the initially very low ion content in this solution, the conductivity increased gradually during incubation, reaching values close to 1.0 $mS \cdot cm^{-1}$ after a longer period of time. This increase clearly indicates the release of ions from the materials into the surrounding solution.

The degree of degradation of the tested materials after 14 days of incubation in various environments is presented in Table 7. Overall, all samples exhibited a noticeable loss of mass, indicating partial degradation of the polymer matrix under the conditions used.

Among the polymer samples (A–C), relatively similar levels of degradation were observed, with values typically ranging from approximately 29% to 40%, depending on the

Table 7. Degree of degradation (%) of the investigated materials after incubation in PBS, artificial saliva, simulated body fluid (SBF), Ringer's solution, and distilled water. Data are presented as mean ± SD (n = 3).

Sample	Degree of degradation (%)				
	PBS	Artificial saliva	SBF	Ringer's solution	Distilled water
A	34.92 ± 0.64	40.23 ± 1.00	32.87 ± 0.56	35.72 ± 0.57	37.71 ± 0.86
B	33.45 ± 0.68	32.37 ± 0.73	29.68 ± 0.57	29.39 ± 0.15	31.13 ± 0.84
C	32.11 ± 1.08	36.41 ± 0.72	30.92 ± 0.35	31.96 ± 0.19	33.94 ± 0.34
A-DCPD	34.13 ± 0.51	35.76 ± 0.27	33.40 ± 0.24	37.87 ± 0.58	38.33 ± 0.99
B-DCPD	34.04 ± 0.32	37.78 ± 0.42	32.56 ± 0.47	38.35 ± 0.92	36.48 ± 0.30
C-DCPD	36.08 ± 0.75	48.63 ± 0.39	41.20 ± 0.45	46.43 ± 0.59	43.82 ± 0.48

incubation environment. Sample A exhibited the highest degree of degradation in artificial saliva (40.23%), while lower values were observed in SBF (32.87%). Samples B and C exhibited a slightly lower and more uniform degree of degradation, particularly in SBF and Ringer's solution, where values remained below 32%.

The inclusion of the ceramic phase (DCPD) had a clear effect on the materials' degradation behavior. Overall, the polymer-ceramic composites exhibited higher degradation values compared to their counterparts containing only polymer with polysaccharide. This effect was particularly pronounced in the C-DCPD sample, which exhibited the highest degree of degradation among all materials, reaching 48.63% in artificial saliva and over 41% in SBF. Similarly, the B-DCPD and A-DCPD samples also exhibited increased degradation in most media compared to the B and A samples, respectively. The increased rate of degradation observed in samples containing DCPD could be related to the presence of a ceramic phase, which may affect the polymer network structure and facilitate water penetration and ion exchange processes.

The type of incubation medium also had a significant impact on the degradation process. Among all the tested media, artificial saliva consistently resulted in the highest degradation values for most samples. In contrast, SBF generally led to the lowest levels of degradation, suggesting a stabilizing effect of this medium on the material's structure. PBS and distilled water exhibited intermediate behavior, while Ringer's solution caused moderate degradation depending on the sample composition. Overall, the results indicate that both the material composition (presence of DCPD) and the type of incubation medium significantly influence the degradation behavior of the developed polymer-ceramic hydrogels.

Surface and Mechanical Characteristics

Analysis of surface morphology (Fig. 7) revealed a clear influence of composition on the topography of the materials. In the polymer samples, it was observed that as the PVP content increased, the surface became more wavy and irregular. This phenomenon can be attributed to differences in the behaviour of the components during the drying process, in particular the greater water retention capacity of PVP and the resulting greater volume shrinkage [47]. This leads to the formation of surface stresses and a surface buckling effect, which is not visible in sample A, where PEG dominates. Apart from this, the polymeric surfaces are similar. Samples containing DCPD exhibit a distinctly developed, rough morphology associated with the presence of mineral phase particles. In these samples, the influence of the polymer composition on the surface topography is less pronounced, and the morphology is determined by the ceramic. The morphological images of all composites are similar to one another and exhibit roughness, which may promote potential cell adhesion. Surface roughness enhances the adsorption of proteins derived from the biological environment, which mediate the initial interactions between the cell and the material [48,49].

The surface roughness parameters of the tested materials before and after incubation in various environments are presented in Table 8. Roughness was characterized using the arithmetic mean roughness (Ra) and the maximum profile height (Rz), which provide quantitative information on average surface irregularities and the height difference between the peak and valley of the surface profile, respectively. Representative surface topographies, 3D models, and roughness profiles are shown in Fig. 8, while the corresponding profiles after incubation are included in the **Supplementary Figs. 6–9**.

Prior to incubation, all samples exhibited relatively moderate roughness values, with Ra ranging from approximately 2.89 μm to 11.30 μm. The highest initial roughness was observed for sample A (Ra = 11.30 μm, Rz = 68.36 μm), while samples B and C showed lower values, indicating a more uniform and smoother surface morphology. The DCPD-containing samples exhibited comparable or slightly lower initial roughness, suggesting that the incorporation of the ceramic phase did not significantly increase surface irregularities at this stage.

After incubation, a significant change in surface topography was observed, particularly for the polymer-based samples (A–C), which exhibited a higher variability of roughness depending on the incubation medium compared to the polymer-ceramic composites. Among the purely polymeric materials, sample A showed the most pronounced changes in surface morphology. In particular, in-

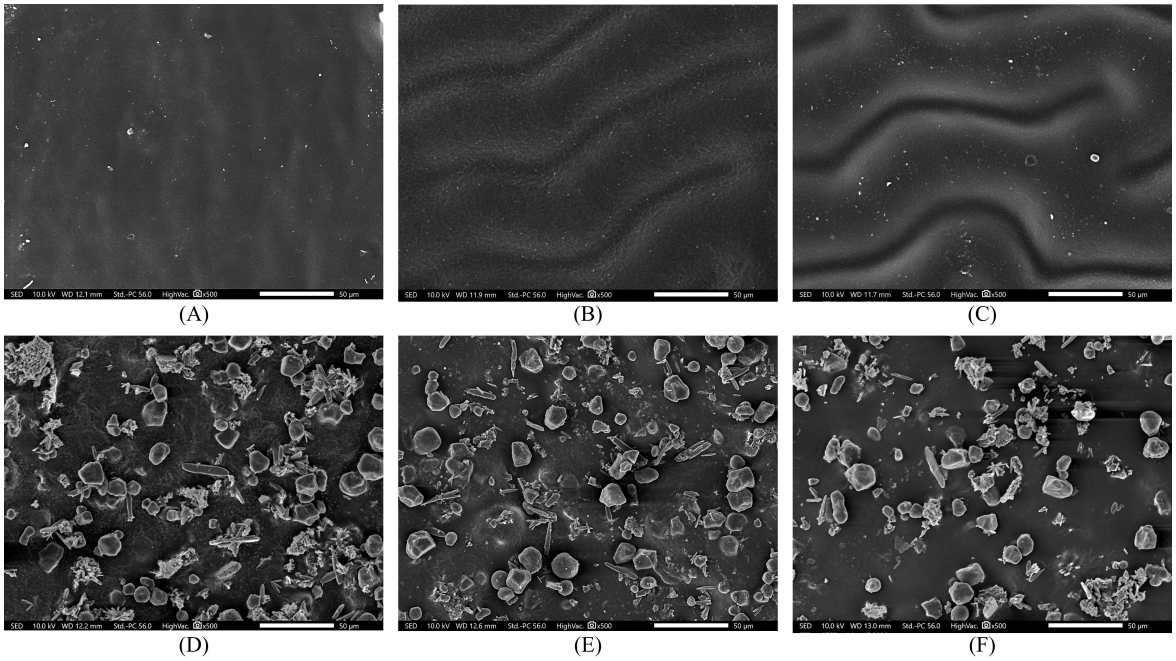

Fig. 7. Surface morphology of polymeric materials. (**A**) sample A; (**B**) sample B; (**C**) sample C, and composite materials (**D**) sample A-DCPD; (**E**) sample B-DCPD; (**F**) sample C-DCPD, before incubation. 500× magnification, scale bar = 50 μm.

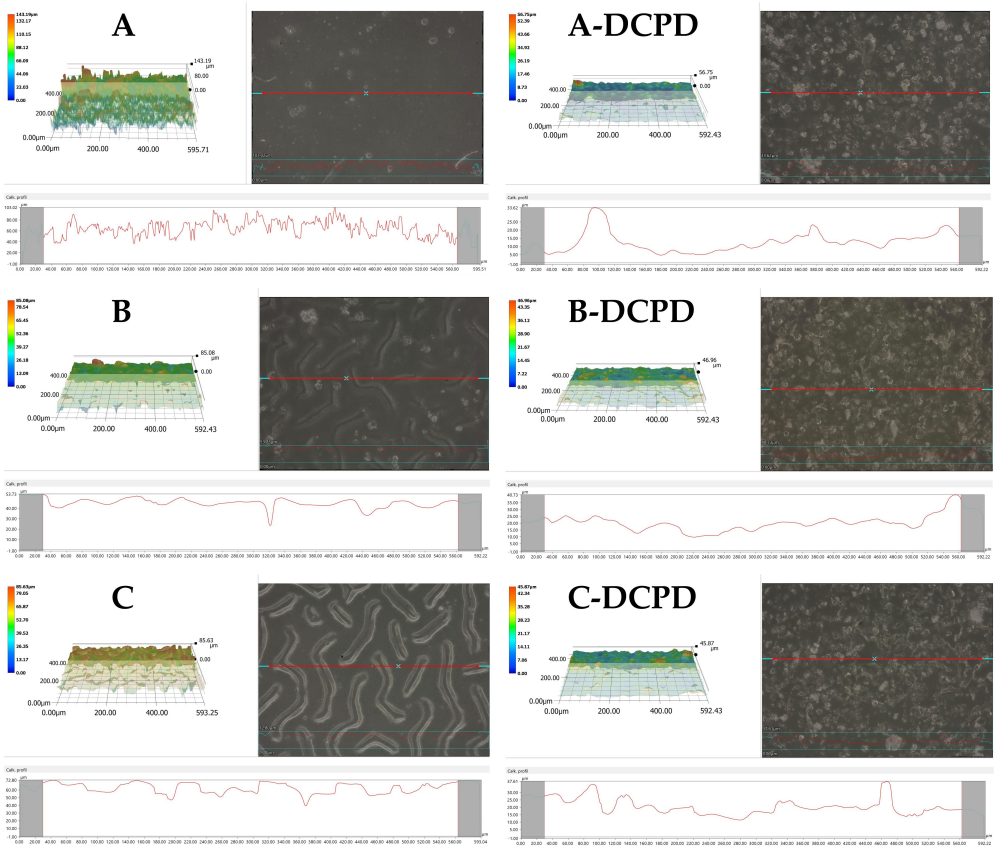

Fig. 8. Representative optical images, 3D surface reconstructions, and corresponding roughness profiles of the investigated polymer and polymer-ceramic samples before incubation. All images were acquired at 500× magnification. The red line indicates the profile line used for roughness analysis.

Table 8. Surface roughness parameters (Ra and Rz) of the investigated materials before incubation and after incubation in PBS, artificial saliva, SBF, and Ringer's solution.

Sample	Before incubation		Incubation fluid							
			PBS		Artificial saliva		SBF		Ringer's solution	
	Ra (μm)	Rz (μm)	Ra (μm)	Rz (μm)	Ra (μm)	Rz (μm)	Ra (μm)	Rz (μm)	Ra (μm)	Rz (μm)
A	11.30	68.36	3.54	16.74	37.81	256.00	16.15	105.12	19.03	81.34
B	2.89	29.67	10.60	65.84	13.45	68.67	17.67	74.93	3.06	14.50
C	6.04	33.46	3.37	13.00	6.06	26.89	13.88	76.12	3.38	12.56
A-DCPD	4.61	28.91	4.93	21.14	5.55	20.13	5.57	22.40	2.81	12.65
B-DCPD	3.92	30.94	2.57	15.25	9.74	55.13	3.90	17.61	2.50	19.58
C-DCPD	4.07	26.22	3.81	17.72	15.42	70.13	3.29	14.02	2.23	9.19

cubation in artificial saliva resulted in a substantial increase in both Ra and Rz values (Ra = 37.81 μm, Rz = 256.00 μm), indicating significant surface development and the formation of pronounced irregularities. Elevated roughness parameters were also observed for this sample after incubation in SBF (Ra = 16.15 μm, Rz = 105.12 μm) and Ringer's solution (Ra = 19.03 μm, Rz = 81.34 μm), suggesting that the polymer matrix was susceptible to structural changes in aqueous environments. In contrast, samples B and C displayed lower roughness values and more moderate changes across the tested media. For sample B, the Ra values ranged from 3.06 μm (Ringer's solution) to 17.67 μm (SBF), while the corresponding Rz values varied between 14.50 μm and 74.93 μm. Sample C exhibited relatively low Ra values in most media, particularly in PBS and Ringer's solution (Ra = 3.37 μm and 3.38 μm, respectively), indicating a comparatively stable and smoother surface morphology even after incubation. The incorporation of the ceramic phase (DCPD) noticeably influenced the surface characteristics of the materials. The polymer-ceramic composites (A-DCPD, B-DCPD, and C-DCPD) generally exhibited lower and more stable roughness parameters compared to their polymer-only counterparts. Importantly, the changes in roughness after incubation were significantly less pronounced than in the case of purely polymeric samples. For instance, sample A-DCPD showed reduced roughness in artificial saliva (Ra = 5.55 μm, Rz = 20.13 μm) relative to sample A, indicating that the presence of the ceramic phase effectively limited the formation of large surface irregularities. Similarly, samples B-DCPD and C-DCPD demonstrated relatively low Ra values across most incubation media, ranging from 2.23 μm to 9.74 μm. The lowest roughness values were observed for sample C-DCPD after incubation in Ringer's solution (Ra = 2.23 μm, Rz = 9.19 μm), indicating a particularly smooth and stable surface morphology.

Hardness Measurement

The results of the hardness measurements are presented in Fig. 9. It can be observed that as the PVP content increased, a systematic increase in hardness was observed, which clearly indicates a significant influence of composition on the mechanical properties of the materials. Sample A, in which PEG was dominant, exhibited the lowest hardness, which can be attributed to the high mobility of the PEG chains and their plasticising effect. Conversely, increasing the PVP content led to a gradual stiffening of the structure, likely due to stronger interchain interactions and reduced polymer chain mobility, resulting in a more compact, deformation-resistant network. PVP is known to enhance the mechanical strength of hydrogel systems, while PEG typically contributes to increased chain mobility and flexibility of the polymer network [50,51]. The addition of DCPD increased hardness in all analysed samples, confirming the effectiveness of the ceramic additive as a reinforcing agent. A correlation was observed between the polymer composition and the DCPD content. In samples with higher PVP content, the reinforcing effect was strongest, suggesting better phase compatibility and more effective stress transfer at the phase boundary. The stiffer and more ordered PVP network likely promotes better 'anchoring' of the ceramic particles, limiting their relative movement within the matrix and increasing the effectiveness of mechanical reinforcement. In contrast, in PEG-rich materials like sample A, the greater flexibility and mobility of the chains may lead to weaker interactions with the mineral phase and thus to less effective stress transfer.

In Vitro Biological Response

The biological response of MC3T3-E1 cells to the tested materials was evaluated using indirect (NRU and XTT) as well as direct cytotoxicity assays, and a proliferation assay (Fig. 10). The results of the indirect cytotoxicity assays showed that all tested materials exhibited good cellular compatibility, and cell viability values consistently exceeded the 70% threshold specified in ISO 10993-5 [52]. Both the NRU and XTT assays showed comparable trends after 24 and 48 hours of exposure to material extracts, indicating that leachable components did not adversely affect either lysosomal function or mitochondrial metabolic activity. In most cases, cell viability remained at a level similar to or higher than that of the negative control, suggesting a low cytotoxic potential of the developed systems. Slight differences were observed between the indi-

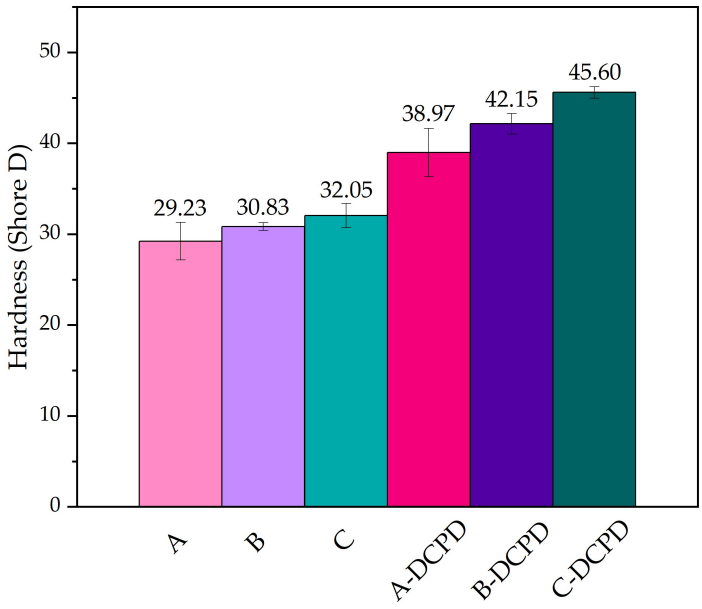

Fig. 9. Hardness of obtained materials. Data are presented as mean ± SD (n = 4).

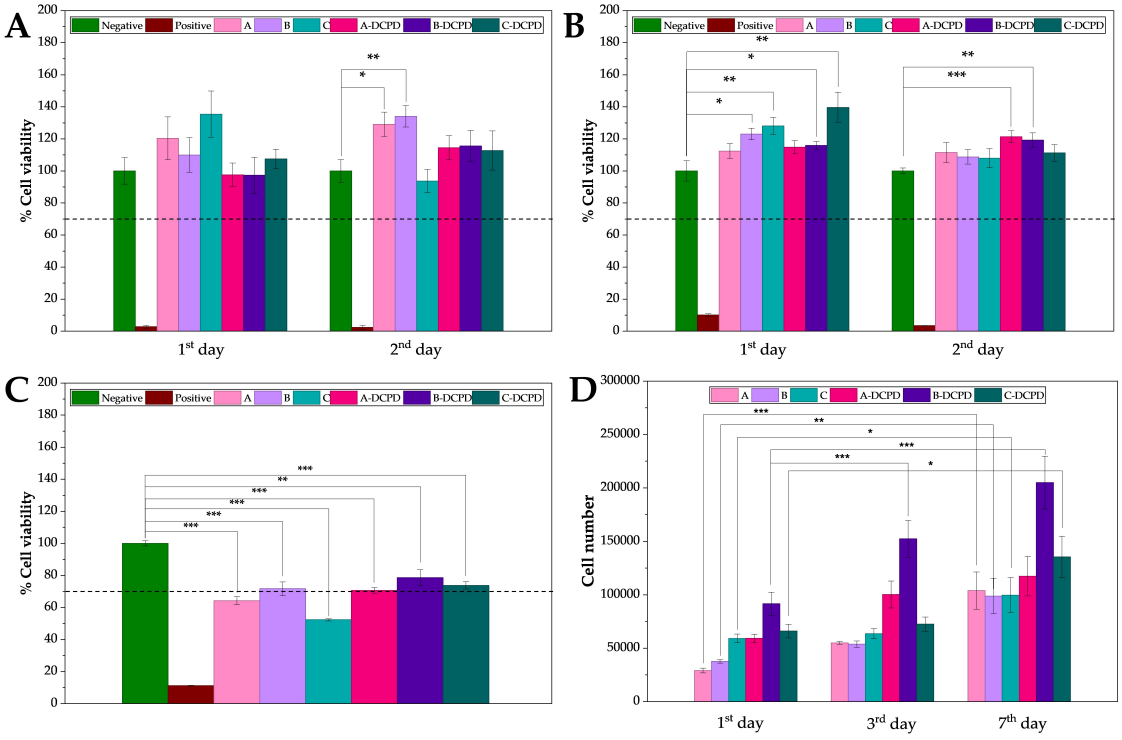

Fig. 10. Biological response of MC3T3-E1 cells to the investigated materials. (**A**) indirect cytotoxicity (NRU), (**B**) indirect cytotoxicity (XTT), (**C**) direct cytotoxicity (XTT), and (**D**) cell proliferation determined by the XTT assay at 1, 3, and 7 days. Data are presented as mean ± SE (n = 6). Statistical analysis for panels A–C was performed using one-way ANOVA, whereas proliferation data (**D**) were analysed using two-way ANOVA followed by Tukey's post hoc test. Statistical significance is denoted as *$p < 0.05$, **$p < 0.01$, and *$p < 0.001$.

vidual compositions, particularly when comparing samples containing only polymer with polymer-ceramic composites. Materials containing DCPD exhibited essentially the same or moderately increased cell viability, especially at longer incubation times. This behavior may be associated with the presence of calcium and phosphate ions released from the ceramic phase, which positively influence osteoblast activity. The results of the direct cytotoxicity test further confirmed the beneficial biological properties of these materials. MC3T3-E1 cells cultured directly on the surface of the samples maintained high viability after 48 hours of incubation, indicating that the materials did not cause adverse effects upon direct contact. The polymer-ceramic composites showed results comparable to or slightly better than those of samples containing only polymer, suggesting that the inclusion of DCPD did not negatively affect the interactions between the cells and the material.

In addition to being compatible with cells, all tested materials promoted cell proliferation over time. An XTT-based proliferation assay revealed a clear, time-dependent increase in cell numbers between days 1, 3, and 7 of culture. This gradual increase confirms that these materials provide a suitable microenvironment for cell adhesion, survival, and growth. Importantly, samples containing DCPD demonstrated more pronounced cell growth at later time points, indicating increased proliferative activity compared to systems containing only polymer. The results obtained indicate that the developed polymer-ceramic composites are not only non-toxic to cells but also promote cellular activity. Two-way ANOVA revealed significant effects of both material composition ($F = 8.36$, $p < 0.0001$) and time ($F = 45.68$, $p < 0.0001$) on MC3T3-E1 proliferation. A significant interaction between these factors was also observed ($F = 1.98$, $p = 0.044$), indicating that the proliferation profile over time depended on the material formulation. Among all investigated materials, the B-DCPD composite exhibited the highest cell numbers after 7 days of culture and showed a significant increase in proliferation already after 3 days compared with day 1, suggesting particularly favourable conditions for cell growth and colonisation of the material surface. The results obtained indicate that the developed polymer-ceramic composites are not only non-toxic to cells but also promote cellular activity.

To evaluate early cell adhesion, MC3T3-E1 cells cultured on the investigated materials for 24 hours were examined by SEM (Fig. 11). Adherent cells were observed on all samples, indicating favorable surface properties for initial cell attachment. The DCPD-containing composites appeared to promote more extensive cell spreading and closer contact with the material surface, suggesting enhanced early cell-material interactions.

SEM observations after direct contact with MC3T3-E1 cells revealed the presence of cells on all samples examined. The results are presented in Fig. 12, where the purple arrows indicate representative cell-covered regions. Measurements were carried out on cross-sections of the materials, revealing the presence of cells within the examined regions of the samples. In the case of samples A-C, the number of cells observed was lower than for the DCPD samples. The composites exhibited better interactions between the cells and the material, with some of them exhibiting partial spreading and stronger adhesion to the surface. The rough surface of the composite promotes mechanical anchoring of the cells. Among the tested materials, the B-DCPD and C-DCPD samples exhibited the most visible early cell-material interactions, as indicated by the higher number of cells imaged.

Additional SEM/EDS analysis was performed for selected regions of the B and B-DCPD samples following direct cytotoxicity testing (**Supplementary Fig. 10** and **Supplementary Table 3**). The analyzed cell-covered regions on the B-DCPD surface exhibited detectable calcium and phosphorus signals, whereas no calcium was identified in the corresponding regions of the B sample. The presence of these elements may indicate the formation of calcium phosphate-containing deposits associated with cell-material interactions.

SEM observations after 7 days of culture revealed the presence of MC3T3-E1 cells on all the materials tested, confirming their ability to support cell adhesion. The images are presented in Fig. 13, with representative cell-covered regions marked by purple arrows. In the case of the polymer samples A-C, the cells were observed as elongated “filament-like” structures. The composite samples containing DCPD exhibited a greater number of adhered cells, which formed extensive structures across the entire surface. Among the composites studied, the B-DCPD sample appeared to provide the most favourable surface for cell adhesion, as indicated by the more extensive spread of cells and the formation of a greater number of continuous cellular structures. In the case of the composite samples, this behaviour can be attributed to the combined influence of surface roughness and the presence of the calcium phosphate phase, which likely promotes adsorption and provides additional anchorage sites for the cells.

Additional SEM/EDS analysis of selected cell-covered regions (**Supplementary Fig. 11** and **Supplementary Table 4**) revealed increased calcium and phosphorus content on the B-DCPD surface compared to the corresponding polymeric material. The presence of these elements may suggest the formation of calcium phosphate-containing deposits associated with the cell-material interface after 7 days of culture.

Discussion

This study presents a rational strategy for designing polymer-ceramic hydrogels, in which the interaction between polymer composition, suspension stability, and photopolymerization enables precise control over swelling, ion release, and surface properties, which ultimately deter-

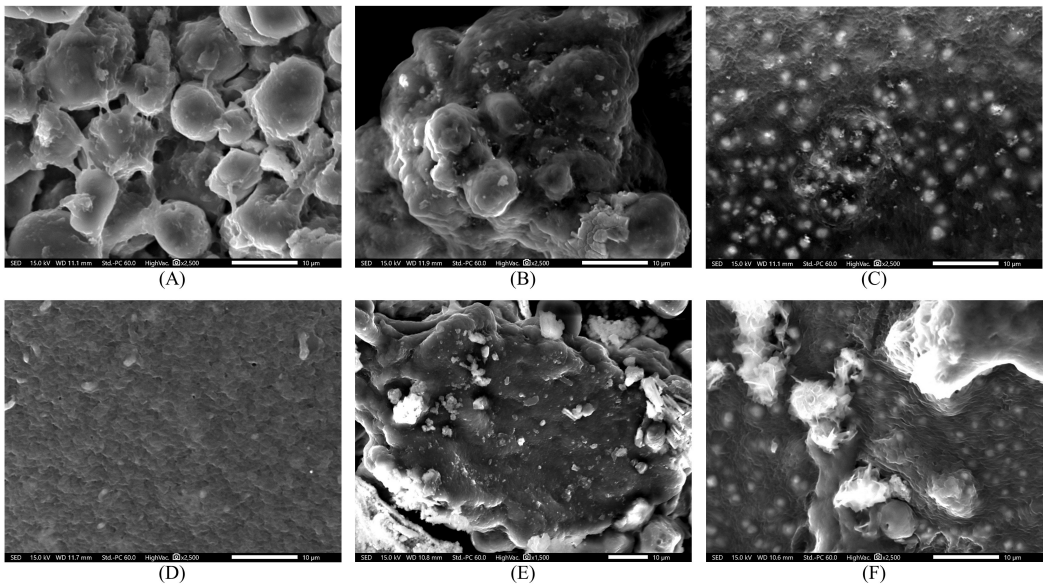

Fig. 11. Representative SEM images of MC3T3-E1 cells cultured on the test materials for 24 hours. (**A**) sample A; (**B**) sample B; (**C**) sample C; (**D**) sample A-DCPD; (**E**) sample B-DCPD; and (**F**) sample C-DCPD. Scale bar = 10 μm.

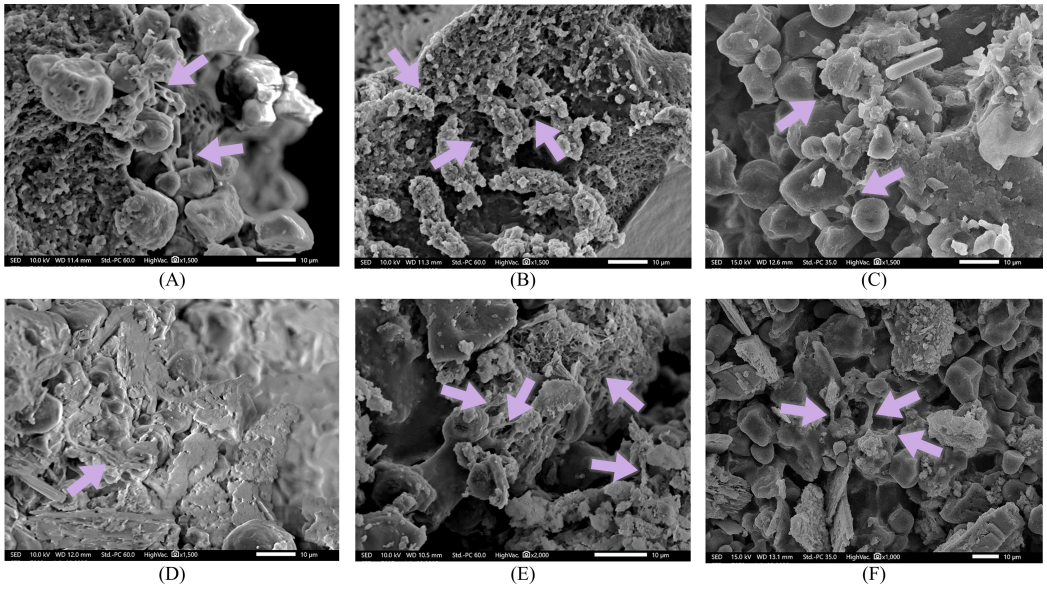

Fig. 12. Visualisation of cells on the materials after direct cytotoxicity test. (**A**) sample A; (**B**) sample B; (**C**) sample C, and composite materials (**D**) sample A-DCPD; (**E**) sample B-DCPD; (**F**) sample C-DCPD. Representative cell-covered regions are indicated by purple arrows. Scale bar = 10 μm.

mines the biological response of osteoblasts. Importantly, the successful production of homogeneous composites required careful optimization of both the polymer concentration and the photopolymerization conditions. The choice of a 15% PVP/PEG system was not arbitrary, but stemmed from the need to find a balance between suspension stability and processability. Lower polymer content led to rapid sedimentation and phase separation, while higher concentrations increased viscosity to a level that hindered processing. This underscores the often-overlooked importance of precursor suspension engineering in determining the final properties of the material. FT-IR analysis confirmed not only successful photopolymerisation but also the formation of a hybrid network in which the polymer and ceramic phases are not merely physically mixed but interact at the molecular level. The reduction of C = C bands indicates efficient crosslinking, while the presence and stability of phosphate groups confirm that DCPD retains its structural identity within the network [53]. The observed spectral shifts suggest interfacial interactions between the polymer chains and the ceramic phase, which are known to influence stress transfer, degradation behaviour, and bi-

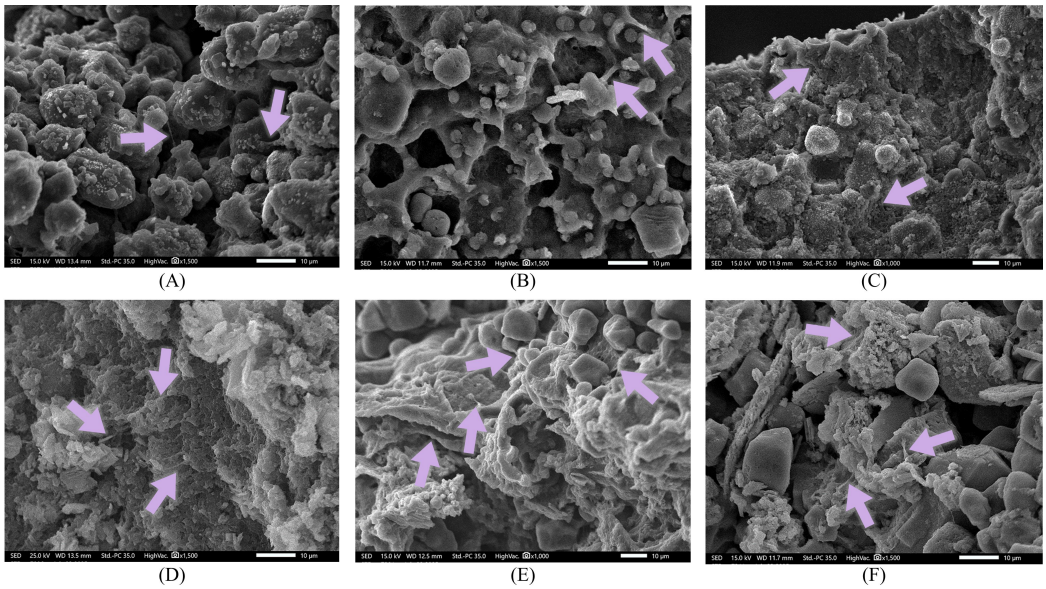

Fig. 13. Visualisation of cells on the materials after direct proliferation test. (**A**) sample A; (**B**) sample B; (**C**) sample C, and composite materials (**D**) sample A-DCPD; (**E**) sample B-DCPD; (**F**) sample C-DCPD. Representative cell-covered regions are indicated by purple arrows. Scale bar = 10 μm.

ological performance [54,55]. The swelling behaviour provides direct evidence of how polymer composition governs network architecture and transport properties. PEG-rich systems exhibited significantly higher swelling due to their hydrophilicity and chain mobility, whereas PVP-rich systems formed more compact and less permeable networks [45,46]. Crucially, the introduction of DCPD altered not only the magnitude but also the kinetics of swelling, indicating restricted chain mobility and increased diffusion path tortuosity [56]. This demonstrates that the ceramic phase acts as a structural regulator, limiting excessive swelling while maintaining sufficient permeability for biological interactions. Such control over swelling is essential, as it directly affects nutrient transport, ion exchange, and cellular infiltration. Changes in pH and conductivity further confirm that these materials are not passive scaffolds but actively interact with their environment. The increase in conductivity clearly indicates the release of ions, most likely Ca^{2+} and PO_4^{3-} ions, resulting from the dissolution of DCPD. This behavior is characteristic of bioactive calcium phosphate systems, which undergo controlled dissolution and reprecipitation processes in an aqueous environment [57]. Importantly, the absence of drastic pH changes suggests that ion release occurs in a controlled manner, thereby avoiding cytotoxic effects. This balance between activity and stability is essential for biomedical applications. Furthermore, the degradation characteristics further confirm the role of DCPD as a multifunctional component. While systems containing only the polymer exhibited more pronounced structural changes, the composites were characterized by increased stability, indicating that the ceramic phase reinforces the matrix. At the same time, the partial dissolution of DCPD contributes to the sustained release of ions, linking the degradation process directly to bioactivity. This dual function-mechanical reinforcement combined with biochemical stimulation-is a hallmark of advanced biomaterials.

Surface properties are another key factor determining biological properties. Increasing the PVP content led to the formation of wrinkled and heterogeneous surfaces due to differential drying and shrinkage effects [47], while PEG-rich systems remained relatively smooth. However, the introduction of DCPD dominated the surface morphology, causing pronounced roughness. It is known that such topographical features enhance protein adsorption and mediate cell adhesion by increasing surface energy and the number of available binding sites [58,59]. Therefore, the ceramic phase not only modifies the bulk properties but also determines the interfacial characteristics of the material. SEM observations show that these physicochemical properties directly translate into biological effects. Polymer-ceramic composites exhibited increased cell adhesion, proliferation, and distribution compared to systems containing only polymer. Cells were present not only on the surface but also in cross-sections, indicating the materials' ability to support cell infiltration – an essential prerequisite for tissue regeneration. After long-term culture, the composite samples exhibited extensive and interconnected cellular networks, in contrast to the more limited and elongated morphology observed in materials containing only polymer.

Among all the systems studied, B-DCPD proved to be the most promising candidate, exhibiting an optimal balance between swelling, structural stability, and surface development. This balance appears to be critical, as exces-

sive swelling or overly compact structures can negatively affect interactions between cells and the material. The excellent performance of this formulation underscores the importance of precisely adjusting polymer ratios in hybrid systems. The results of biological assays strongly support these observations. All substances were found to be non-cytotoxic, as confirmed by both NRU and XTT assays, indicating that lysosomal and mitochondrial functions were preserved. More importantly, the presence of DCPD consistently increased cell viability and proliferation, particularly over longer time periods. This effect can be attributed to the release of Ca^{2+} and PO_4^{3-} ions, which are known to regulate osteoblast activity, signaling pathways, and matrix mineralization [60,61]. Proliferation data, together with SEM observations, indicate that the materials support not only cell survival but also cell adhesion, infiltration into the scaffold, and proliferation. These effects are likely associated with the surface chemistry and bioactivity imparted by the DCPD addition, as well as surface properties such as roughness [62,63].

In summary, the results indicate a clear relationship between processing conditions, network architecture, physicochemical behavior, and biological response. The developed system serves as an example of how the integration of synthetic polymers, natural polysaccharides, and bioactive ceramics can be used to design multifunctional biomaterials with tailored properties.

Conclusions

Herein, it is demonstrated that a photocrosslinked PEG-PVP-pullulan composite reinforced with DCPD may be effectively engineered as a multifunctional biomaterial, exhibiting properties that can be tailored for potential bone and osteochondral tissue engineering applications. Through optimisation of polymer composition, precursor suspension stability, and photocrosslinking conditions, homogeneous composites with controlled swelling and degradation behavior. The incorporation of DCPD significantly enhanced the performance of the materials by improving structural stability, increasing surface roughness, and enabling the release of calcium and phosphate ions, which may contribute to cellular activity relevant to bone tissue regeneration. Subsequently, the tunable polymer matrix provides a hydrated and compliant environment that is favorable for cartilage tissue regeneration. This combination suggests that the developed systems may be suitable candidates for further investigation in osteochondral tissue engineering. All investigated materials were cytocompatible and supported cell proliferation, confirming their suitability for further biological evaluation. Notably, the B-DCPD composition exhibited the most balanced combination of physicochemical and biological properties, indicating that precise control over polymer-ceramic ratios is crucial for achieving optimal performance in osteochondral systems. Importantly, the results highlight that both material composition and processing parameters play a key role in determining the final biological response, providing a framework for the rational design of hybrid biomaterials for osteochondral applications.

Despite these promising findings, further studies are required to fully validate the potential of the developed materials. In particular, advanced *in vitro* studies, including co-culture systems and differentiation assays relevant to osteochondral tissue regeneration, as well as *in vivo* investigations in osteochondral defect models, are necessary to assess their regenerative performance and integration with host tissue. The presented materials offer a promising platform for the development of gradient or bilayer osteochondral scaffolds.

List of Abbreviations

α-MEM, alpha minimum essential medium; DCPD, dicalcium phosphate dihydrate; DPBS, Dulbecco's phosphate-buffered saline; ECM, extracellular matrix; EDTA, ethylenediaminetetraacetic acid; FBS, fetal bovine serum; FT-IR, fourier-transform infrared spectroscopy; NRU, neutral red uptake; PBS, phosphate-buffered saline; PEG, poly(ethylene glycol); PEGDA, poly(ethylene glycol) diacrylate; PMS, phenazine methosulfate; PVP, poly(vinylpyrrolidone); SBF, simulated body fluid; SEM, scanning electron microscopy; Tris, tris(hydroxymethyl)aminomethane; XTT, 22,3-Bis(2-methoxy-4-nitro-5-sulfophenyl)-2H-tetrazolium-5-carboxanilide inner salt.

Availability of Data and Materials

Data for this article are available at the Mendeley Data repository at https://data.mendeley.com/datasets/crjx79hdks/2.

Author Contributions

KN contributed to the Conceptualization, Writing-original draft, Data curation, Formal analysis, Investigation, Methodology, Resources, Software, Validation, Visualization; DS contributed to the Formal analysis, Writing-original draft, Software; KH contributed to the Methodology, Writing-review & editing; ASK contributed to Writing-review & editing, Funding acquisition, Project administration, Supervision. All authors read and approved the final manuscript. All authors agree to be accountable for all aspects of the work in ensuring that questions related to the accuracy or integrity of any part of the work are appropriately investigated and resolved.

Ethics Approval and Consent to Participate

Not applicable.

Acknowledgments

The work was supported by the National Science Centre, Poland, under the research project "Hierarchical approaches for osteochondral tissue engineering", no. UMO-2022/45/B/ST8/02557.

Funding

This research was funded in whole by the National Science Centre, Poland, grant no. UMO-2022/45/B/ST8/02557. For the purpose of Open Access, the author has applied a CC-BY public copyright licence to any Author Accepted Manuscript (AAM) version arising from this submission.

Conflict of Interest

The authors declare no conflict of interest.

Supplementary Material

Supplementary Figs. 1–4 can be found in the supplementary material, available online at https://doi.org/10.22203/eCM.v058a12.

References

[1] Sharif MU, Aslam HM, Iftakhar T, Abdullah M. Pathophysiology of cartilage damage in knee osteoarthritis and regenerative approaches toward recovery. Journal of Bone and Joint Diseases. 2024; 39: 32–44. https://doi.org/10.4103/jbjd.jbjd_2_24.

[2] Wang M, Wu Y, Li G, Lin Q, Zhang W, Liu H, *et al*. Articular cartilage repair biomaterials: strategies and applications. Materials Today. Bio. 2024; 24: 100948. https://doi.org/10.1016/j.mtbio.2024.100948.

[3] Mordor Intelligence. Cartilage Repair/Regeneration Market Size & Share Analysis–Growth Trends and Forecast (2026–2031). Hyderabad (India): Mordor Intelligence. 2026. Available at: https://www.mordorintelligence.com/industry-reports/cartilage-repairregeneration-market (Accessed: 24 March 2026).

[4] Lesage C, Lafont M, Guihard P, Weiss P, Guicheux J, Delplace V. Material-Assisted Strategies for Osteochondral Defect Repair. Advanced Science. 2022; 9: e2200050. https://doi.org/10.1002/advs.202200050.

[5] Oliveira S, Hinckel BB, Silva FS, Carvalho Ó, Leal A. A guide to articular cartilage functioning: a comprehensive review, current challenges and mechanobiological solutions. Progress in Biomedical Engineering. 2025; 7: 032009. https://doi.org/10.1088/2516-1091/ade83a.

[6] Kutaish H, Klopfenstein A, Obeid Adorisio SN, Tscholl PM, Fucentese S. Current trends in the treatment of focal cartilage lesions: a comprehensive review. EFORT Open Reviews. 2025; 10: 203–212. https://doi.org/10.1530/EOR-2024-0083.

[7] Familiari F, Ferrua P, Fedele G, Carlisi G, Russo R, Randelli PS, *et al*. Surgical management of chondral defects of the patellofemoral joint: a narrative review. Joints. 2024; 2: e1339. https://doi.org/10.26355/joints_202412_1339.

[8] Li CS, Xu Y, Li J, Qin SH, Huang SW, Chen XM, *et al*. Ultramodern natural and synthetic polymer hydrogel scaffolds for articular cartilage repair and regeneration. Biomedical Engineering Online. 2025; 24: 13. https://doi.org/10.1186/s12938-025-01342-3.

[9] Morouço P, Fernandes C, Lattanzi W. Challenges and innovations in osteochondral regeneration: Insights from biology and inputs from bioengineering toward the optimization of tissue engineering strategies. Journal of Functional Biomaterials. 2021; 12: 17. https://doi.org/10.3390/jfb12010017.

[10] Barthold JE, Cai L, McCreery KP, Fischenich KM, Eckstein KN, Ferguson VL, *et al*. Integrative cartilage repair using acellular allografts for engineered structure and surface lubrication in vivo. NPJ Regenerative Medicine. 2024; 9: 25. https://doi.org/10.1038/s41536-024-00367-x.

[11] Hameed H, Faheem S, Paiva-Santos AC, Sarwar HS, Jamshaid M. A Comprehensive Review of Hydrogel-Based Drug Delivery Systems: Classification, Properties, Recent Trends, and Applications. AAPS PharmSciTech. 2024; 25: 64. https://doi.org/10.1208/s12249-024-02786-x.

[12] Sánchez-Cid P, Jiménez-Rosado M, Romero A, Pérez-Puyana V. Novel Trends in Hydrogel Development for Biomedical Applications: A Review. Polymers. 2022; 14: 3023. https://doi.org/10.3390/polym14153023.

[13] Zhang W, Zha K, Hu W, Xiong Y, Knoedler S, Obed D, *et al*. Multifunctional hydrogels: advanced therapeutic tools for osteochondral regeneration. Biomaterials Research. 2023; 27: 76. https://doi.org/10.1186/s40824-023-00411-9.

[14] Kong H, Zheng J, Han J, Meng X, Li X, Wang X, *et al*. The crosstalk among macrophages, chondrocytes and mesenchymal stem cells in osteoarthritis: the role of extracellular vesicles. Stem Cell Research & Therapy. 2025; 16: 553. https://doi.org/10.1186/s13287-025-04659-x.

[15] Wang X, Zeng J, Gan D, Ling K, He M, Li J, *et al*. Recent Strategies and Advances in Hydrogel-Based Delivery Platforms for Bone Regeneration. Nano-Micro Letters. 2024; 17: 73. https://doi.org/10.1007/s40820-024-01557-4.

[16] Rumon MMH, Akib AA, Sarkar SD, Khan MAR, Uddin MM, Nasrin D, *et al*. Polysaccharide-Based Hydrogels for Advanced Biomedical Engineering Applications. ACS Polymers Au. 2024; 4: 463–486. https://doi.org/10.1021/acspolymersau.4c00028.

[17] Nanda D, Behera D, Pattnaik SS, Behera AK. Advances in natural polymer-based hydrogels: synthesis, applications, and future directions in biomedical and environmental fields. Discover Polymers. 2025; 2: 6. https://doi.org/10.1007/s44347-025-00017-5.

[18] Krishnan Y, Sampath S. Biopolymers and synthetic polymeric materials in wound healing: cellular mechanisms and therapeutic potential. Discover Materials. 2025; 5: 254. https://doi.org/10.1007/s43939-025-00435-z.

[19] Gong L, Zhu J, Yang Y, Qiao S, Ma L, Wang H, *et al.* Effect of polyethylene glycol on polysaccharides: From molecular modification, composite matrixes, synergetic properties to embeddable application in food fields. Carbohydrate Polymers. 2024; 327: 121647. https://doi.org/10.1016/j.carbpol.2023.121647.

[20] Bano H, Jusoh N, Suhaimi NH. Synergistic effects of polyvinylpyrrolidone and graphene oxide in thin film nanocomposite membranes for oily wastewater treatment via forward osmosis process. Scientific Reports. 2025; 15: 27372. https://doi.org/10.1038/s41598-025-11383-2.

[21] Niziołek K, Słota D, Sobczak-Kupiec A. Polysaccharide-Based Composite Systems in Bone Tissue Engineering: A Review. Materials. 2024; 17: 4220. https://doi.org/10.3390/ma17174220.

[22] Lu P, Ruan D, Huang M, Tian M, Zhu K, Gan Z, *et al.* Harnessing the potential of hydrogels for advanced therapeutic applications: current achievements and future directions. Signal Transduction and Targeted Therapy. 2024; 9: 166. https://doi.org/10.1038/s41392-024-01852-x.

[23] Chávez-Herrera D, Rangel-Villanueva E, Salazar-Hernández M, Talavera-Lopez A, Ardila A AN, Hernández-Soto R, *et al*. Morphology-Dependent Transformation of Dicalcium Phosphate Dihydrate (DCPD) to Octacalcium Phosphate (OCP) and Its Stability in Simulated Physiological Fluids. Molecules. 2025; 30: 3631. https://doi.org/10.3390/molecules30173631.

[24] Lee J, Bae JS, Kim YI, Yoo KH, Yoon SY. Synthesis, Characterization, and Biological Performances of Magnesium-Substituted Di-

calcium Phosphate Anhydrous. Materials. 2024; 17: 4605. https://doi.org/10.3390/ma17184605.

[25] Shi Y, Tao W, Yang W, Wang L, Qiu Z, Qu X, *et al.* Calcium phosphate coating enhances osteointegration of melt electrowritten scaffold by regulating macrophage polarization. Journal of Nanobiotechnology. 2024; 22: 47. https://doi.org/10.1186/s12951-024-02310-0.

[26] Wei S, Ma JX, Xu L, Gu XS, Ma XL. Biodegradable Materials for Bone Defect Repair. Military Medical Research. 2020; 7: 54. https://doi.org/10.1186/s40779-020-00280-6.

[27] Sharma A, Kokil GR, He Y, Lowe B, Salam A, Altalhi TA, *et al*. Inorganic/organic combination: Inorganic particles/polymer composites for tissue engineering applications. Bioactive Materials. 2023; 24: 535–550. https://doi.org/10.1016/j.bioactmat.2023.01.003.

[28] Niziołek K, Słota D, Ronowska A, Sobczak-Kupiec A. Calcium phosphate biomaterials modified with Mg^{2+} or Mn^{2+} ions: Structural, chemical, and biological characterization. Ceramics International. 2025; 51: 23542–23558. https://doi.org/10.1016/j.ceramint.2025.03.042.

[29] Słota D, Szwed-Georgiou A, Włodarczyk M, Krupa A, Rudnicka K, Niziołek K, *et al*. Bioactive coating with clindamycin, VEGF-165, and TGF-β1 for supporting bone tissue regeneration. Biomaterials Science. 2025; 13: 6085–6097. https://doi.org/10.1039/d5bm00637f.

[30] Słota D, Urbaniak MM, Tomaszewska A, Niziołek K, Włodarczyk M, Florkiewicz W, *et al*. Crosslinked hybrid polymer/ceramic composite coatings for the controlled release of clindamycin. Biomaterials Science. 2024; 12: 5253–5265. https://doi.org/10.1039/d4bm00055b.

[31] International Organization for Standardization (ISO). ISO 10993-5:2009. Biological Evaluation of Medical Devices–Part 5: Tests for In Vitro Cytotoxicity. Geneva, Switzerland: International Organization for Standardization. 2009. Available at: https://www.iso.org/standard/36406.html (Accessed: 24 March 2026).

[32] International Organization for Standardization (ISO). ISO 10993-12:2021. Biological Evaluation of Medical Devices–Part 12: Sample Preparation and Reference Materials. Geneva, Switzerland: International Organization for Standardization. 2021. Available at: https://www.iso.org/standard/75769.html (Accessed: 24 March 2026).

[33] Haraźna K, Fricker AT, Konefał R, Medaj A, Zimowska M, Leszczyński B, *et al*. Physicochemical, structural and biological characterisation of poly(3-hydroxyoctanoate) supplemented with diclofenac acid conjugates – Harnessing the potential in the construction of materials for skin regeneration processes. International Journal of Biological Macromolecules. 2024; 268: 131476. https://doi.org/10.1016/j.ijbiomac.2024.131476.

[34] Sundararajan S, Kumar A, Chakraborty BC, Samui AB, Kulkarni PS. Poly(ethylene glycol) (PEG)-modified epoxy phase-change polymer with dual properties of thermal storage and vibration damping. Sustainable Energy & Fuels. 2018; 2: 688–697. https://doi.org/10.1039/c7se00552k.

[35] Visan AI, Popescu-Pelin G, Gherasim O, Mihailescu A, Socol M, Zgura I, *et al*. Long-term evaluation of dip-coated PCL-blend-PEG coatings in simulated conditions. Polymers. 2020; 12: 717. https://doi.org/10.3390/polym12030717.

[36] Pereira ED, Cerruti R, Fernandes E, Peña L, Saez V, Pinto JC, *et al*. Influence of PLGA and PLGA-PEG on the dissolution profile of oxaliplatin. Polímeros. 2016; 26: 137–143. https://doi.org/10.1590/0104-1428.2323.

[37] Franca T, Goncalves D, Cena C. ATR-FTIR spectroscopy combined with machine learning for classification of PVA/PVP blends in low concentration. Vibrational Spectroscopy. 2022; 120: 103378. https://doi.org/10.1016/j.vibspec.2022.103378.

[38] Safo IA, Werheid M, Dosche C, Oezaslan M. The role of polyvinylpyrrolidone (PVP) as a capping and structure-directing agent in the formation of Pt nanocubes. Nanoscale Advances. 2019; 1: 3095–3106. https://doi.org/10.1039/c9na00186g.

[39] Abdelghany AM, Elamin NY, Younis S, Ayaad DM. Polyvinyl pyrrolidone/carboxymethyl cellulose (PVP/CMC) polymer composites containing CuO nanoparticles synthesized via laser ablation in liquids. Journal of Molecular Liquids. 2024; 403: 124857. https://doi.org/10.1016/j.molliq.2024.124857.

[40] Uysal E, Dursun HN, Güler R, Takmaz U, Küt A, Çeri M, *et al.* Waste refractory brick material added chitosan/oxidized pullulan complex gel production and removal of heavy metals from waste water. Scientific Reports. 2024; 14: 26229. https://doi.org/10.1038/s41598-024-72187-4.

[41] Wani SM, Masoodi FA, Mir SA, Khanday FA. Pullulan production by Aureobasidium pullulans MTCC 1991 from apple pomace and its characterization. Food Bioscience. 2023; 51: 102254. https://doi.org/10.1016/j.fbio.2022.102254.

[42] Kizildag N. Pullulan Films with PCMs: Recyclable Bio-Based Films with Thermal Management Functionality. Coatings. 2023; 13: 414. https://doi.org/10.3390/coatings13020414.

[43] Florkiewicz W, Słota D, Placek A, Pluta K, Tyliszczak B, Douglas TEL, *et al*. Synthesis and Characterization of Polymer-Based Coatings Modified with Bioactive Ceramic and Bovine Serum Albumin. Journal of Functional Biomaterials. 2021; 12: 21. https://doi.org/10.3390/jfb12020021.

[44] Petrakova NV, Teterina AY, Mikheeva PV, Akhmedova SA, Kuvshinova EA, Sviridova IK, *et al.* In Vitro Study of Octacalcium Phosphate Behavior in Different Model Solutions. ACS Omega. 2021; 6: 7487–7498. https://doi.org/10.1021/acsomega.0c06016.

[45] Yang X, Dargaville BL, Hutmacher DW. Elucidating the molecular mechanisms for the interaction of water with polyethylene glycol-based hydrogels: Influence of ionic strength and gel network structure. Polymers. 2021; 13: 845. https://doi.org/10.3390/polym13060845.

[46] Franco P, De Marco I. The use of poly(N-vinyl pyrrolidone) in the delivery of drugs: A review. Polymers. 2020; 12: 1114. https://doi.org/10.3390/polym12051114.

[47] Wen J, Liu W, Xie Z, Lou C, Yang X. Effects of PVP incorporation on the properties of injection-molded high-performance ceramics with PEG-based binders. Ceramics International. 2018; 44: 2718–2726. https://doi.org/10.1016/j.ceramint.2017.10.227.

[48] Yang Y, Knust S, Schwiderek S, Qin Q, Yun Q, Grundmeier G, *et al*. Protein adsorption at nanorough titanium oxide surfaces: The importance of surface statistical parameters beyond surface roughness. Nanomaterials. 2021; 11: 357. https://doi.org/10.3390/nano11020357.

[49] Hou R, Willumeit-Römer R, Garamus VM, Frant M, Koll J, Feyerabend F. Adsorption of Proteins on Degradable Magnesium–Which Factors are Relevant? ACS Applied Materials & Interfaces. 2018; 10: 42175–42185. https://doi.org/10.1021/acsami.8b17507.

[50] Bashir S, Hina M, Iqbal J, Rajpar AH, Mujtaba MA, Alghamdi NA, *et al.* Fundamental Concepts of Hydrogels: Synthesis, Properties, and Their Applications. Polymers. 2020; 12: 2702. https://doi.org/10.3390/polym12112702.

[51] D'Errico G, De Lellis M, Mangiapia G, Tedeschi A, Ortona O, Fusco S, *et al.* Structural and mechanical properties of UV-photo-cross-linked poly(N-vinyl-2-pyrrolidone) hydrogels. Biomacromolecules. 2008; 9: 231–240. https://doi.org/10.1021/bm7008137.

[52] Haraźna K, Cichoń E, Skibiński S, Witko T, Solarz D, Kwiecień I, *et al.* Physicochemical and biological characterisation of diclofenac oligomeric poly(3-hydroxyoctanoate) hybrids as β-TCP ceramics modifiers for bone tissue regeneration. International Journal of Molecular Sciences. 2020; 21: 9452. https://doi.org/10.3390/ijms21249452.

[53] Imani M, Sharifi S, Mirzadeh H, Ziaee F. Monitoring of polyethylene glycol diacrylate-based hydrogel formation by real-time NMR spectroscopy. Iranian Polymer Journal. 2007; 16: 13–20.

[54] Jaggessar A, Shahali H, Mathew A, Yarlagadda PKDV. Biomimicking nano and micro-structured surface fabrication for an-

tibacterial properties in medical implants. Journal of Nanobiotechnology. 2017; 15: 64. https://doi.org/10.1186/s12951-017-0306-1.

[55] Zhang L, Pei J, Wang H, Shi Y, Niu J, Yuan F, *et al*. Facile Preparation of Poly(lactic acid)/Brushite Bilayer Coating on Biodegradable Magnesium Alloys with Multiple Functionalities for Orthopedic Application. ACS Applied Materials & Interfaces. 2017; 9: 9437–9448. https://doi.org/10.1021/acsami.7b00209.

[56] Słota D, Jampilek J, Sobczak-Kupiec A. Hybrid Coatings Based on Polyvinylpyrrolidone/Polyethylene Glycol Enriched with Collagen and Hydroxyapatite: Incubation Studies and Evaluation of Mechanical and Physiochemical Properties. Journal of Functional Biomaterials. 2024; 15: 62. https://doi.org/10.3390/jfb15030062.

[57] Alanazi AA, Abdulaziz F, Alyami M, Alotibi S, Sakka S, Mallouh SA, *et al*. The Effect of Full-Scale Exchange of Ca^{2+} with Zn^{2+} Ions on the Crystal Structure of Brushite and Its Phase Composition. Biomimetics. 2023; 8: 333. https://doi.org/10.3390/biomimetics8040333.

[58] Lee WH, Loo CY, Rohanizadeh R. A review of chemical surface modification of bioceramics: Effects on protein adsorption and cellular response. Colloids and Surfaces B: Biointerfaces. 2014; 122: 823–834. https://doi.org/10.1016/j.colsurfb.2014.07.029.

[59] Hamraoui A. Cell adhesion and surface interactions: A comprehensive review of surface energy, wettability, and topography effects. AIP Advances. 2025; 15: 090702. https://doi.org/10.1063/5.0280399.

[60] Hou X, Zhang L, Zhou Z, Luo X, Wang T, Zhao X, *et al*. Calcium Phosphate-Based Biomaterials for Bone Repair. Journal of Functional Biomaterials. 2022; 13: 187. https://doi.org/10.3390/jfb13040187.

[61] Kosuge M, Hazama K, Suzuki K, Aizawa M. Osteoblast and osteoclast responses to chelate-setting calcium phosphate cements with different solubilities. Biomaterials and Biosystems. 2026; 21: 100129. https://doi.org/10.1016/j.bbiosy.2026.100129.

[62] Li L, Crosby K, Sawicki M, Shaw LL, Wang Y. Effects of Surface Roughness of Hydroxyapatite on Cell Attachment and Proliferation. Journal of Biotechnology & Biomaterials. 2012; 2: 150. https://doi.org/10.4172/2155-952X.1000150.

[63] Padilla S, Benito-Garzón L, Enciso Sanz S, Garzón-Gutiérrez A, García Carrodeguas R, Rodríguez MA, *et al*. Novel Osteoinductive and Osteogenic Scaffolds of Monetite, Amorphous Calcium Phosphate, Hydroxyapatite, and Silica Gel: Influence of the Hydroxyapatite/Monetite Ratio on Their in Vivo Behavior and on Their Physical and Chemical Properties. ACS Biomaterials Science & Engineering. 2020; 6: 3440–3453. https://doi.org/10.1021/acsbiomaterials.9b01689.

Editor's note: The Scientific Editors responsible for this paper were Chris Evans and Kelong Fan.

Received: 26th March 2026; **Accepted**: 15th July 2026; **Published**: 31st August 2026